

Probabilistic Estimates of the Maximum Norm of Random Neumann Fourier Series

Dirk Blömker*

Philipp Wacker†

Thomas Wanner‡

April 1, 2024

Abstract

We study the maximum norm behavior of L^2 -normalized random Fourier cosine series with a prescribed large wave number. Precise bounds of this type are an important technical tool in estimates for spinodal decomposition, the celebrated phase separation phenomenon in metal alloys. We derive rigorous asymptotic results as the wave number converges to infinity, and shed light on the behavior of the maximum norm for medium range wave numbers through numerical simulations. Finally, we develop a simplified model for describing the magnitude of extremal values of random Neumann Fourier series. The model describes key features of the development of maxima and can be used to predict them. This is achieved by decoupling magnitude and sign distribution, where the latter plays an important role for the study of the size of the maximum norm. Since we are considering series with Neumann boundary conditions, particular care has to be placed on understanding the behavior of the random sums at the boundary.

*Universität Augsburg, 86135 Augsburg, Germany, dirk.bloemker@math.uni-augsburg.de

†Universität Augsburg, 86135 Augsburg, Germany, phkwacker@gmail.com

‡George Mason University, Fairfax VA 22030, USA, twanner@gmu.edu

Contents

1	Introduction	2
2	Moment-Based Probabilistic Bounds	6
2.1	Random Fourier Cosine Sums	7
2.2	Bounds on the Moments	10
2.3	Probabilistic Maximum Norm Bounds	12
3	Boundary Behavior and Sign Forcing	13
3.1	Random Fourier Cosine Sums with Forced Signs	13
3.2	The Role of the Left Endpoint of the Domain	18
3.3	The Behavior at the Remaining Points	20
4	Modeling Extreme Values	21
4.1	The Typical Oscillation Magnitude	21
4.2	A Model for the Magnitude of Extreme Values	25
4.3	Growth Rate of the Maximum Norm	27
4.4	Generalization to Higher Dimensions	31
	References	33

1 Introduction

Random series of functions play a significant role in many branches of mathematics and have been studied extensively. Of particular interest in a number of applications is the problem of estimating the maximum norm of random series. For example, in quantum chaos applications the maximum norm of the eigenfunctions of the Laplacian on bounded domains is a measure for localization effects, and it was shown in [1] that one can estimate these norms of deterministic eigenfunctions through random superpositions of plane waves and using methods due to Kahane [12].

This interplay between stochastic techniques and deterministic applications can also be seen in other contexts. Consider for example one of the standard models for phase separation in binary alloys which is due to Cahn and Hilliard [5, 6]. They proposed the fourth-order parabolic partial differential equation

$$\partial_t u = -\Delta(\varepsilon^2 \Delta u + h(u)) \quad \text{in } G, \quad (1)$$

subject to homogeneous Neumann boundary conditions $\partial_\nu u = \partial_\nu \Delta u = 0$ on ∂G , and for some sufficiently smooth domain $G \subset \mathbb{R}^d$. In this model, the unknown function u is an order parameter which represents the concentration difference of the two alloy components, i.e., values of u close to ± 1 represent the pure components, while values in between correspond to mixtures, with $u = 0$ implying equal concentrations of both components. Moreover, the small parameter $\varepsilon > 0$ is a measure for interaction length which is usually on an atomistic length scale, and the nonlinearity is the negative derivative of a double-well potential. A typical

example is $h(u) = u - u^3$, while the h in original work of Cahn and Hilliard had logarithmic poles.

If one observes the evolution of the Cahn-Hilliard model originating at some almost constant homogeneous state $u(0, \cdot) \approx m$, and if the initial concentration difference m satisfies the condition $h'(m) > 0$, then it is well-known that provided sufficiently small $\epsilon > 0$ (1) exhibits spontaneous phase separation through a process called spinodal decomposition. The resulting dynamics of the phase variable u exhibits the formation of complicated and intricate patterns, which are generated by the local convergence of the function values of u to ± 1 , while at the same time keeping the number of separating interfaces as small as possible, see for example [3] and the references therein. From a mathematical point of view, spinodal decomposition in the classical Cahn-Hilliard model (1) has been studied in a series of papers [15, 16, 18, 19] through deterministic methods, and they provide an explanation for both the observed complicated patterns and their generation. In particular, it is shown that the Cahn-Hilliard equation exhibits surprising linear behavior even far from the constant stationary state $u \equiv m$, and [18, 19] provide lower bounds for the region of linear behavior. Unfortunately, however, these lower bounds turn out to be suboptimal.

It was shown in [20] that optimal lower bounds can be obtained, if instead of the deterministic estimates used in [18, 19] one employs a probabilistic approach. More precisely, the suboptimality of the deterministic results is due to the possibility of large ratios between the maximum norm and the $L^2(G)$ -norm of functions representing spinodally decomposed patterns, since the deterministic approach needs to incorporate the value of these ratios for all possible patterns. In practice, however, the ratios are reasonably small, and by studying random Fourier series in combination with randomly chosen initial conditions for the deterministic problem (1) one can show that for “typical” initial conditions linear behavior prevails up to much larger distances from the homogeneous state. For more details, see [11, 20].

As a model, the deterministic Cahn-Hilliard equation (1) ignores thermal fluctuations which are present in any material. This can be resolved by adding a stochastic additive term, see for example [7, 14], and leads to the stochastic Cahn-Hilliard-Cook model

$$\partial_t u = -\Delta(\epsilon^2 \Delta u + h(u)) + \partial_t W \quad \text{in } G, \quad (2)$$

which is again considered subject to Neumann boundary conditions $\partial_\nu u = \partial_\nu \Delta u = 0$ on ∂G , and for some sufficiently smooth domain $G \subset \mathbb{R}^d$. While the nonlinearity h and the interaction parameter ϵ are as before, the additive noise term $\partial_t W$ is the derivative of a small Q -Wiener process W , which will be described in more detail below. Ideally, one would expect space-time white noise with a small noise strength, which is on the order of an atomistic length scale, too. For a survey of the phase separation dynamics of the Cahn-Hilliard-Cook model (2) see for example [3].

Spinodal decomposition can also be observed in the stochastic Cahn-Hilliard model, and some of the above-mentioned results could be extended to the case of (2). More precisely, in [2] it was shown that results analogous to [15, 16] hold, while [4] generalizes the approach of [18, 19]. We would like to stress that even though the basic explanation of spinodal decomposition as a phenomenon driven by unexpectedly linear behavior remains, the proof techniques used in the stochastic setting are completely different.

Despite the above results, a complete description of spinodal decomposition which generalizes the approach described in [20] to the stochastic case remains elusive, and we now describe this somewhat surprising fact in more detail. During spinodal decomposition, an initially flat surface $u \approx m$ separates and closely follows the linearized dynamics for unexpectedly large times. In the stochastic setting, the linearized dynamics near the constant solution $u \equiv m$ is described by the evolution equation

$$\partial_t u = Au + \partial_t W \quad \text{in } G, \quad (3)$$

where the linearized operator is given by $A = -\varepsilon^2 \Delta^2 - h'(m)\Delta$, subject to Neumann boundary conditions and average mass zero. Since m is constant, this operator is self-adjoint and has a complete orthonormal system of eigenfunctions $e_k \in L^2(G)$, for $k \in \mathbb{N}$, with associated eigenvalues

$$\lambda_k = \mu_k (h'(m) - \varepsilon^2 \mu_k) \quad \text{for } k \in \mathbb{N}. \quad (4)$$

One can easily see that the eigenfunctions e_k are the eigenfunctions of the negative Laplacian subject to homogeneous Neumann boundary conditions, with corresponding ordered eigenvalues $0 < \mu_1 \leq \mu_2 \leq \dots \rightarrow \infty$. It is well known [10] that the solution of (3) starting at zero is the stochastic convolution

$$W_A(t) = \int_0^t e^{(t-s)A} dW(s) = \sum_{k \in \mathbb{N}} \alpha_k \int_0^t e^{(t-s)\lambda_k} dB_k(s) \cdot e_k, \quad (5)$$

where the second identity holds for independent Brownian motions B_k if the Q -Wiener process has a joint eigenbase with A such that $Qe_k = \alpha_k^2 e_k$, which for simplicity of discussion we assume throughout this paper.

But why can the probabilistic method used in [20] not easily be applied in the stochastic setting? In the deterministic case, we studied random initial conditions u_0 , which are selected in such a way that their ratio of maximum norm and $L^2(G)$ -norm is small. Then the solution of the linearized equation is given by $e^{tA}u_0$, and this allows us to obtain estimates on the norm ratios along the solution due to the differentiability of the solution with respect to time. In contrast, in the stochastic Cahn-Hilliard-Cook setting, the linearized solution always starts at zero, and the probabilistic aspects enter through the above representation of the stochastic convolution — and the previous approach of bounding the norm ratios cannot easily be applied.

Motivated by the above discussion the present paper is concerned with obtaining a better understanding of when random Fourier series of the type given in (5) exhibit small ratios between their maximum norm and their $L^2(G)$ -norm. We are interested in particular in characterizations which would allow us to extend the results of [20] to the stochastic partial differential equation case. More precisely, we consider the following situation, which is based on the available spinodal decomposition explanations.

Return for the moment to the eigenvalue formula presented in (4). This so-called *dispersion relation* shows how the eigenvalues λ_k of the linearized Cahn-Hilliard operator can be computed from the eigenvalues $\mu_k \geq 0$ of the negative Laplacian subject to homogeneous Neumann boundary conditions. If we define the quadratic polynomial $p(s) = s \cdot (h'(m) - \varepsilon^2 s)$,

then one clearly has $\lambda_k = p(\mu_k)$ for all $k \in \mathbb{N}$. We would like to point out that the polynomial p is positive between its two zeros at $s = 0$ and $s = h'(m)/\varepsilon^2$, i.e., any value of μ_k in this interval gives rise to a positive eigenvalue $\lambda_k > 0$. These positive eigenvalues are of course responsible for the instability of the homogeneous state, and in fact, the *most positive eigenvalues* λ_k are the driving force for pattern formation during spinodal decomposition. One can readily see that the quadratic polynomial p achieves its maximum $\lambda_{\max} = h'(m)^2/(4\varepsilon^2)$ at $s = h'(m)/(2\varepsilon^2)$, and therefore superpositions of the eigenfunctions e_k which correspond to values $\mu_k \approx h'(m)/(2\varepsilon^2)$ accurately describe the microstructures observed during phase separation, see again [15, 16, 18, 19]. We now choose a constant $0 \ll \gamma < 1$ and define

$$\Lambda := \{k \in \mathbb{N} : \lambda_k > \gamma \lambda_{\max}\} , \quad \text{where} \quad \lambda_{\max} = \frac{h'(m)^2}{4\varepsilon^2} .$$

Since the eigenvalues μ_k are ordered by their size, there exist suitable integers $1 \leq k^\ominus \leq k^\oplus$ such that Λ can be rewritten as

$$\Lambda = \{k \in \mathbb{N} : k^\ominus \leq k \leq k^\oplus\} \quad \text{with} \quad k^\oplus - k^\ominus \sim \varepsilon^{-d} \quad \text{as} \quad \varepsilon \rightarrow 0 , \quad (6)$$

where the last proportionality is due to standard results on the asymptotic distribution of Laplacian eigenvalues on bounded domains $G \subset \mathbb{R}^d$, see for example [8]. In [15, 16, 18, 19], the finite-dimensional function space which is spanned by the eigenfunctions e_k for $k \in \Lambda$ is called the *dominating subspace*, and the functions in this space exhibit the characteristic patterns which are observed during spinodal decomposition. Furthermore, it was shown in these papers that solutions of the Cahn-Hilliard model which originate close to the homogeneous state are very likely to stay close to the dominating subspace, and [20] uncovered that most functions in the dominating subspace exhibit small maximum- $L^2(G)$ -norm ratios. As mentioned before, this is the principal reason for the unexpectedly linear behavior observed during spinodal decomposition.

Based on the above discussion, the present paper focuses on the behavior of the stochastic convolution in the invariant dominating subspace. More precisely, let $P_\Lambda : L^2(G) \rightarrow L^2(G)$ denote the orthogonal projection onto the dominating subspace, then we have

$$P_\Lambda W_A(t) = \sum_{k \in \Lambda} \alpha_k c_k \cdot e_k \quad \text{with} \quad c_k = \int_0^t e^{(t-s)\lambda_k} dB_k(s) .$$

Note that due to Itô's isometry the random variables c_k for $k \in \Lambda$ are real-valued Gaussian random variables with mean zero and variance

$$\mathbb{E} c_k^2 = \int_0^t e^{(t-s)2\lambda_k} ds = \frac{1}{2\lambda_k} (1 - e^{-2\lambda_k t}) \approx \frac{1}{2\lambda_k} \approx \frac{2\varepsilon^2}{h'(m)^2}$$

for times $t \gg 1/\lambda_{\max}$ which on the order ε^2 . Here we have used the fact that $\lambda_k > 0$ for all eigenvalues which correspond to indices in Λ and that γ is close to one. Moreover, we used that spinodal decomposition usually happens on a time-scale of order $\varepsilon^2 \ln(\varepsilon^{-1})$, see [2].

If we assume that the noise process acts on each of these modes with the same intensity, then also the constants α_k are of the same size. After normalization, in the remainder of this

paper we therefore study random sums of the form

$$f(x) = \sum_{k \in \Lambda} c_k e_k(x) ,$$

where the coefficients c_k are independent and identically distributed standard Gaussian random variables with mean zero and variance one. Our point of view is that sums of this form can act as a surrogate for the mild solution of the linearized Cahn-Hilliard-Cook equation in the dominant subspace. For the random functions f , we study the size of their $L^\infty(G)$ -norms in relation to their $L^2(G)$ -norms. While the above simplification removes the time dependence from the problem, our study focuses on understanding the maximum norm behavior of f in a way which we believe will allow for a straightforward inclusion of time later on. More precisely, we will show that

$$\mathbb{P} \left(\frac{\|f\|_{L^\infty(G)}}{\|f\|_{L^2(G)}} < C \cdot \log \varepsilon^{-1} \right) \xrightarrow{\varepsilon \rightarrow 0} 1 ,$$

yet in doing so we will shed light on the actual mechanism that controls the size of the maximum norm. This is accomplished through a mixture of analysis, modeling, and numerical simulations. In order to keep the presentation simple, much of the paper concentrates on the one-dimensional case $d = 1$, although we do address extensions to higher dimensions as well.

The remainder of the paper is organized as follows. In Section 2 we introduce the specific one-dimensional setting that is used for most of the paper. In addition, we obtain a first crude estimate for the asymptotic behavior of the maximum norm of f as $\varepsilon \rightarrow 0$ through purely probabilistic means. While this result will provide a first step, it is indirect in nature and does not explain exactly how the maximum norms are generated. This question is addressed in Section 3, where we study the effect of the signs of the random coefficients c_k in the definition of f on the maximum norm. For this, we will have to treat the boundary and the interior of the domain G separately. We show that only equal signs force the worst-case norm behavior, which of course is an extremely rare event. Finally, in Section 4 we try to explain how local extrema are generated, and how this relates to matchings between the signs of the eigenfunctions e_k and their respective random coefficients c_k . In addition, we introduce a simplified model which exhibits the properties of the random function f in relation to the generation of local extreme values. This in turn leads to an intuitive explanation of the behavior of maximum norms of the random functions f . The section closes with generalizations to higher dimensions.

2 Moment-Based Probabilistic Bounds

This section lays the groundwork for our study of the maximum norms of normalized random functions subject to Neumann boundary conditions. In addition to introducing our precise setup, we provide some intuition into the norm ratio behavior. We then review indirect probabilistic approaches for estimating the ratio.

2.1 Random Fourier Cosine Sums

Beginning with this section, we consider only the one-dimensional special case $G = [0, 1]$. Furthermore, we consider the Cahn-Hilliard-Cook model with total mass $m = 0$, i.e., the identity $h'(m) = 1$ holds. In this situation, the eigenfunctions of the negative Laplacian are cosines with varying wave numbers, and one can easily see that after $L^2(0, 1)$ -normalization they are given by $e_k(x) = \sqrt{2} \cos(k\pi x)$, with associated eigenvalues $\mu_k = k^2\pi^2$ for $k \in \mathbb{N}$. Notice that the constant eigenfunction is excluded from consideration, since the Cahn-Hilliard model is usually studied on function spaces which respect the mass constraint. For more details we refer the reader to [15, 16, 18, 19]. One can easily see that the dispersion relation (4) now takes the form

$$\lambda_k = k^2\pi^2 (h'(m) - \varepsilon^2 k^2\pi^2) = k^2\pi^2 - \varepsilon^2 k^4\pi^4 \quad \text{for} \quad k \in \mathbb{N},$$

which provides a direct link between the wave number k of the eigenmode e_k and the associated eigenvalue λ_k of the linearization A of the Cahn-Hilliard equation. Furthermore, a simple calculation shows that the index set for the dominating subspace is given by

$$\Lambda = \{k^\ominus, \dots, k^\oplus\} = \left\{ \left\lceil \frac{\alpha^\ominus}{\varepsilon} \right\rceil, \dots, \left\lfloor \frac{\alpha^\oplus}{\varepsilon} \right\rfloor \right\}, \quad \text{where} \quad \alpha^{\oplus, \ominus} = \sqrt{\frac{1 \pm \sqrt{1 - \gamma}}{2\pi^2}}. \quad (7)$$

As a model for the projected stochastic convolution $P_\Lambda W_A(t)$ in the dominating subspace we consider random weighted sums of the cosine basis functions whose wave numbers lie in Λ . More precisely, we consider the following setting.

Definition 1. For $\gamma \in (0, 1)$ let $\Lambda = \{k^\ominus, \dots, k^\oplus\} = \{\lceil \alpha^\ominus/\varepsilon \rceil, \dots, \lfloor \alpha^\oplus/\varepsilon \rfloor\}$ denote the index set of dominating wave numbers defined in (7). Furthermore, let c_k for $k \in \Lambda$ denote a family of independent and identically distributed standard normal random variables. Then we define a random Fourier cosine sum $f : [0, 1] \rightarrow \mathbb{R}$ via

$$f(x) = \sum_{k \in \Lambda} c_k \sqrt{2} \cos(k\pi x) = \sum_{k \in \Lambda} c_k e_k(x). \quad (8)$$

Notice that the basis functions e_k are orthonormal in $L^2(0, 1)$.

Our goal is to understand the relation between typical maximum norm values of functions f as in (8) and their $L^2(0, 1)$ -norms. As mentioned in the introduction, part of this study will be rigorous, while other parts will be numerical in nature. For the numerical simulations in the remainder of this paper, unless otherwise noted, we assume that

$$\gamma = 0.8, \quad \text{and therefore} \quad \alpha^\ominus \approx 0.16735 \quad \text{and} \quad \alpha^\oplus \approx 0.27077,$$

and we generally pick the ε -values listed in Table 1. In this table, we also list the values of k^\ominus and k^\oplus for each of these cases, as well as the dimension $|\Lambda|$ of the dominating subspace. The final column will be discussed in more detail later on.

Random Fourier cosine sums as defined in Definition 1 usually exhibit highly oscillatory behavior for small values of ε , since the wave numbers of all involved basis functions are

r	$\varepsilon = 10^{-r}$	k^{\ominus}	k^{\oplus}	$ \Lambda $	$2\sqrt{ \Lambda /\pi}$
2.0	0.01	17	27	11	3.7424
2.5	0.003162	53	85	33	6.4820
3.0	0.001	168	270	103	11.4518
3.5	0.0003162	530	856	327	20.4046
4.0	0.0001	1674	2707	1034	36.2840

Table 1: Simulation parameters used throughout the paper. For the shown values of ε , the table lists the bounds k^{\ominus} and k^{\oplus} of the index set Λ defined in (7), as well as its size. The last column will be explained in more detail later.

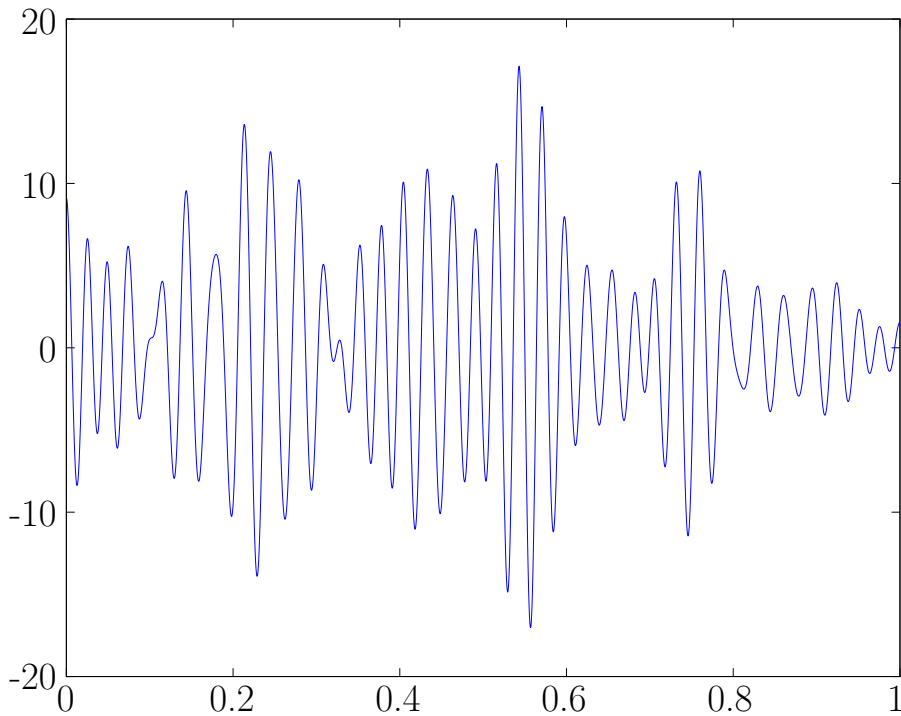


Figure 1: A typical instance of a random Fourier cosine sum f as defined in Definition 1. For the image we chose the parameters $\varepsilon = 10^{-3}$ and $\gamma = 0.8$.

of the order $1/\varepsilon$. In fact, a classical result due to Karlin [13] shows that every f as in (8) contains between k^{\ominus} and k^{\oplus} zeros. This is demonstrated in Figure 1, where we show a sample random Fourier cosine sum for $\varepsilon = 10^{-3}$. Notice that f exhibits fast oscillations at a frequency of order ε with a slow modulation. A fundamental difference to many other studies of random Fourier sums is, that not only the number of terms increases with $\varepsilon \rightarrow 0$, but also the functions over which the sum is taken changes.

As a first step towards understanding the behavior of the maximum norm of f in rela-

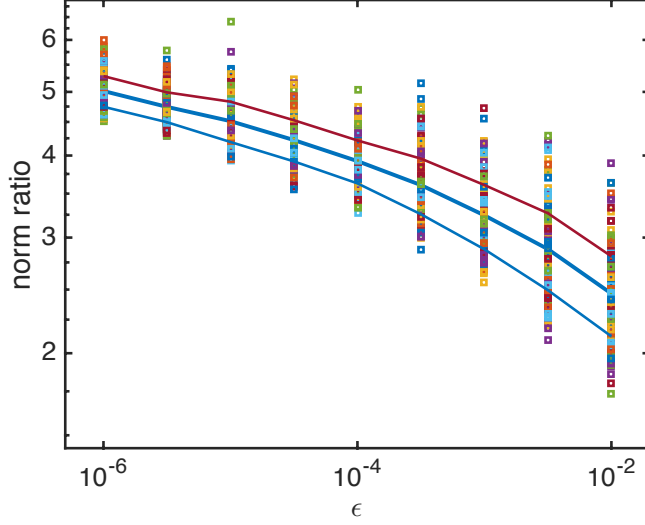


Figure 2: Monte Carlo simulations of random Fourier cosine sums for ε -values between 10^{-6} and 10^{-2} . In each case, the ratio of the maximum norm and the L^2 -norm of the function f is indicated by a square. The thick blue line shows the mean values of the simulations.

tion to its L^2 -norm, we would like to point out that the worst-case behavior can easily be determined, see also [20].

Observation 2 (Worst-Case Behavior). *Consider an arbitrary random Fourier cosine sum as in Definition 1. Since all cosines are uniformly bounded by one, the Cauchy-Schwarz inequality immediately yields the estimate*

$$\frac{\|f\|_{L^\infty(0,1)}}{\|f\|_{L^2(0,1)}} \leq \frac{\sum_{k \in \Lambda} \sqrt{2}|c_k|}{\sqrt{\sum_{k \in \Lambda} c_k^2}} \leq \frac{\sqrt{2} \cdot \sqrt{|\Lambda|} \cdot \sqrt{\sum_{k \in \Lambda} c_k^2}}{\sqrt{\sum_{k \in \Lambda} c_k^2}} = \sqrt{2 \cdot |\Lambda|} \sim \varepsilon^{-1/2}.$$

Moreover, one can easily see, for example by choosing all coefficients c_k equal to one, that both of the above inequalities can be turned into equalities. For this one only has to notice that the cosines attain their maximum value at the left interval endpoint $x = 0$, and therefore we have $\|f\|_{L^\infty(0,1)} = f(0)$ whenever the coefficients c_k are positive for all $k \in \Lambda$.

The observation shows that as we choose ε closer and closer to zero, the norm ratio grows proportional to $\varepsilon^{-1/2}$. In fact, the observation even provides explicit functions f for which this asymptotic behavior is realized.

But what happens in the stochastic setting? How do the ratios behave for typical instances of the random Fourier cosine sum? To gain some intuition, we performed Monte Carlo type simulations for values of ε between 10^{-6} and 10^{-2} , with sample size 250 in each case, and recorded the norm ratio. The results are shown in Figure 2, which also depicts the expected value of the simulations for each ε -value in blue. This leads to the following observation.

Observation 3 (Typical Behavior). *For typical instances of the random Fourier cosine sum f introduced in Definition 1, the norm ratio $\|f\|_{L^\infty(0,1)}/\|f\|_{L^2(0,1)}$ appears to level off as ε*

approaches zero. In addition, the variances observed in the Monte Carlo simulations seem to decrease as ε approaches zero.

This second observation identifies a large disparity between the worst-case and the typical behavior of the norm ratios, and as mentioned in the introduction, this lies at the heart of spinodal decomposition. We would like to point out, however, that one should not expect the norm ratios shown in Figure 2 to converge to a fixed value. In fact, we do anticipate a small logarithmic growth of the norm ratios as $\varepsilon \rightarrow 0$.

2.2 Bounds on the Moments

For the remainder of this section, we briefly review probabilistic estimates for the maximum norms of random Fourier cosine sums. These estimates are indirect in the sense that they do not provide information on which specific instances of f realize the norm bounds.

Probabilistic methods for deriving uniform bounds for Gaussian random functions are well-known. In the following, we present an approach based on fractional Sobolev spaces, which originated in [9]; see also [10]. To adapt this approach to our setting, we first establish an asymptotic moment bound. Rather than giving almost sure bounds for the norm ratio of interest to us, namely $\|f\|_{L^\infty(0,1)}/\|f\|_{L^2(0,1)}$, this first result only provides bounds on the ratio $(\mathbb{E}\|f\|_{L^\infty(0,1)}^p)^{1/p}/(\mathbb{E}\|f\|_{L^2(0,1)}^2)^{1/2}$, which involves the expected values of the norms of the random Fourier cosine sum f .

Theorem 4. *Consider random Fourier cosine sums f as in Definition 1. Then for arbitrary constants $p > 1$ and $0 < \eta < 2$ there exists a constant $C > 0$ which is independent of ε such that*

$$\mathbb{E}\|f\|_{L^\infty(0,1)}^p \leq C \left(\sum_{k \in \Lambda} k^\eta \right)^{p/2} + C |\Lambda|^{p/2}.$$

Note that the constant in the previous theorem will depend very badly on p . It grows faster than exponential, and we will need large p in the sequel.

Before proving the theorem, we demonstrate how it can be used to bound the above-mentioned moment ratio $(\mathbb{E}\|f\|_{L^\infty(0,1)}^p)^{1/p}/(\mathbb{E}\|f\|_{L^2(0,1)}^2)^{1/2}$. Recall that we are interested in the asymptotic behavior as $\varepsilon \rightarrow 0$. In this case, it has already been shown that $|\Lambda| \sim \varepsilon^{-1}$, as well as $k \sim \varepsilon^{-1}$ for all $k \in \Lambda$. This leads to the following bound for the maximum norm moment in terms of ε .

Corollary 5. *Consider random Fourier cosine sums f as in Definition 1. Then for any choice of $p > 1$ and $\delta > 0$ there exists a constant $C > 0$ such that for $0 < \varepsilon \leq 1$ we have*

$$\left(\mathbb{E}\|f\|_{L^\infty(0,1)}^p \right)^{1/p} \leq C \varepsilon^{-\delta/2} \left(\mathbb{E}\|f\|_{L^2(0,1)}^2 \right)^{1/2} = C \varepsilon^{-(1+\delta)/2}.$$

Proof. Let $\eta = \min\{\delta, 1\}$. Then there is a constant $C > 0$ such that for $0 < \varepsilon \leq 1$ we have

$$\mathbb{E}\|f\|_{L^\infty(0,1)}^p \leq C \left(\sum_{k \in \Lambda} k^\eta \right)^{p/2} + C |\Lambda|^{p/2} \leq C \left(\varepsilon^{-p(\eta+1)/2} + \varepsilon^{-p/2} \right) \leq C \varepsilon^{-p(\delta+1)/2}.$$

Moreover, we have already seen that our assumptions on the random coefficients c_k imply the identity $\mathbb{E}\|f\|_{L^2(0,1)}^2 = |\Lambda| \sim \varepsilon^{-1}$, i.e., one has $(\mathbb{E}\|f\|_{L^2(0,1)}^2)^{1/2} \sim \varepsilon^{-1/2}$. Taking the p -th root finally yields the result. \square

We would like to point out that the constant C in both of the previous results is usually not small. In fact, it usually grows exponentially in the moment exponent p . We now turn our attention to the proof of Theorem 4.

Proof of Theorem 4. Our proof is based on the fractional Sobolev spaces $W^{\alpha,p}(G)$, and we refer the reader to [?, 17] for more details. For the moment, recall that for $\alpha \in (0, 1)$ and $G = [0, 1]$ the definition of the $W^{\alpha,p}(G)$ -norm is given by

$$\|u\|_{W^{\alpha,p}}^p = \int_G \int_G \frac{|u(x) - u(y)|^p}{|x - y|^{1+\alpha p}} dx dy + \|u\|_{L^p}^p.$$

Note further that as long as the inequality $\alpha p > 1$ holds, one has the continuous Sobolev embedding $W^{\alpha,p}(G) \subset C^0(\overline{G})$. For sufficiently large $p > 1/\alpha$ we then obtain

$$\mathbb{E}\|f\|_{L^\infty(0,1)}^p \leq C \mathbb{E}\|f\|_{W^{\alpha,p}}^p = C \mathbb{E} \int_0^1 \int_0^1 \frac{|f(x) - f(y)|^p}{|x - y|^{1+\alpha p}} dx dy + C \mathbb{E}\|f\|_{L^p}^p.$$

Note that according to Definition 1, the random variables $f(x)$ and $f(x) - f(y)$ are real-valued Gaussian random variables, as they are the sum of independent Gaussians. Thus we can bound higher moments by the second to obtain the estimate

$$\mathbb{E}\|f\|_{L^\infty(0,1)}^p \leq C \int_0^1 \int_0^1 \frac{(\mathbb{E}|f(x) - f(y)|^2)^{p/2}}{|x - y|^{1+\alpha p}} dx dy + C \int_0^1 (\mathbb{E}|f(x)|^2)^{p/2} dx.$$

One can easily see that

$$\mathbb{E}|f(x)|^2 = 2 \sum_{k \in \Lambda} \cos^2(k\pi x) \leq 2|\Lambda|,$$

and for any $\eta \in (0, 2)$ there exists a constant C_η such that

$$\begin{aligned} \mathbb{E}|f(x) - f(y)|^2 &= 2 \sum_{k \in \Lambda} |\cos(k\pi x) - \cos(k\pi y)|^2 \\ &\leq C_\eta \sum_{k \in \Lambda} |\cos(k\pi x) - \cos(k\pi y)|^\eta \leq C_\eta \sum_{k \in \Lambda} k^\eta \pi^\eta |x - y|^\eta. \end{aligned}$$

Combined, these estimates imply

$$\begin{aligned} \mathbb{E}\|f\|_{L^\infty(0,1)}^p &\leq C \int_0^1 \int_0^1 \frac{\left(C_\eta \sum_{k \in \Lambda} k^\eta \pi^\eta |x - y|^\eta\right)^{p/2}}{|x - y|^{1+\alpha p}} dx dy + C \int_0^1 (|\Lambda|)^{p/2} dx \\ &\leq C \left(\sum_{k \in \Lambda} k^\eta\right)^{p/2} \int_0^1 \int_0^1 |x - y|^{\eta p/2 - 1 - \alpha p} dx dy + C |\Lambda|^{p/2}, \end{aligned}$$

where the constants C depend on p and η . Finally, choose $\eta \in (2\alpha, 2)$ and $p > 1/\alpha$. Then we have $\eta p/2 - 1 - \alpha p > -1$, and the above estimate yields

$$\mathbb{E}\|f\|_{L^\infty(0,1)}^p \leq C \left(\sum_{k \in \Lambda} k^\eta \right)^{p/2} + C|\Lambda|^{p/2}.$$

for some constant $C > 0$. Thus, we have proved the result for large p , which in combination with Hölder's inequality also establishes its validity for smaller values of p . \square

2.3 Probabilistic Maximum Norm Bounds

After the preparations of the last section, we can now finally derive probabilistic bounds on the norm ratio $\|f\|_{L^\infty(0,1)}/\|f\|_{L^2(0,1)}$. These bounds will be true only asymptotically and with high probability. Unfortunately, however, they will not shed any light on which instances of the random Fourier cosine sum f realize the small norm ratios. Moreover, they do not cover the range of moderately small values of ε . This is due to the fact that the involved constants depend in a highly nonlinear way on the parameters q and δ below.

Theorem 6. *Consider random Fourier cosine sums f as in Definition 1. Then for any choice of $\delta > 0$ and any $q > 1$ there exists a constant $C > 0$ such that*

$$\mathbb{P} \left(\|f\|_{L^\infty(0,1)} \leq \varepsilon^{-\delta} \|f\|_{L^2(0,1)} \right) \geq 1 - C\varepsilon^q.$$

As before, the constant C is independent of ε . In other words, with probability close to one the norm ratio $\|f\|_{L^\infty(0,1)}/\|f\|_{L^2(0,1)}$ grows at most like $\varepsilon^{-\delta}$ as $\varepsilon \rightarrow 0$.

Proof. Let $y > 0$ be an arbitrary constant, whose precise value will be fixed later in the proof. Then we obtain

$$\begin{aligned} \mathbb{P} \left(\|f\|_{L^\infty(0,1)} \leq \varepsilon^{-\delta} \|f\|_{L^2(0,1)} \right) &\geq \mathbb{P} \left(\|f\|_{L^\infty(0,1)} \leq \varepsilon^{-\delta} y \text{ and } y \leq \|f\|_{L^2(0,1)} \right) \\ &\geq 1 - \mathbb{P} \left(\|f\|_{L^\infty(0,1)} > \varepsilon^{-\delta} y \right) - \mathbb{P} \left(y > \|f\|_{L^2(0,1)} \right) \\ &\geq 1 - \mathbb{E} \|f\|_{L^\infty(0,1)}^p \cdot \left(\frac{\varepsilon^\delta}{y} \right)^p - \mathbb{P} \left(y^2 > \|f\|_{L^2(0,1)}^2 \right). \end{aligned}$$

The remaining two terms will be bounded separately. For the second one, we can use the fact that the random variable $\|f\|_{L^2(0,1)}^2$ is chi-squared distributed with $N = |\Lambda| \sim \varepsilon^{-1}$ degrees of freedom. Using the explicit representation of its density, one then obtains

$$\begin{aligned} \mathbb{P} \left(y^2 > \|f\|_{L^2(0,1)}^2 \right) &= \int_0^{y^2} \frac{x^{N/2-1} e^{-x/2}}{2^{N/2} \Gamma(N/2)} dx \leq \int_0^{y^2} \frac{x^{N/2-1}}{2^{N/2} \Gamma(N/2)} dx \\ &= \frac{(y^2)^{N/2}}{2^{N/2} \Gamma(\frac{N}{2} + 1)} \leq C N^{-1/2} \left(\frac{ey^2}{N} \right)^{N/2}, \end{aligned}$$

where we used Stirling's formula for the last inequality. Thus, this probability is exponentially small in ε as long as y is not too large. More precisely, if we now define

$$y = \sqrt{\frac{|\Lambda|}{2e}} \sim \varepsilon^{-1/2},$$

then $\varepsilon y^2/N = 1/2$, and the probability $\mathbb{P}(y^2 > \|f\|_{L^2(0,1)}^2)$ decays exponentially fast in ε . We now turn our attention to the first term in the first estimate. Using Corollary 5 one obtains

$$\mathbb{E}\|f\|_{L^\infty(0,1)}^p \cdot \left(\frac{\varepsilon^\delta}{y}\right)^p \leq C\varepsilon^{-p(1+\delta)/2} \cdot \varepsilon^{p(\delta+1/2)} \leq C\varepsilon^{\delta p/2}.$$

Choosing $p > 2q/\delta$ completes the proof of the theorem. \square

3 Boundary Behavior and Sign Forcing

3.1 Random Fourier Cosine Sums with Forced Signs

While for the asymptotic regime $\varepsilon \rightarrow 0$ the results of the last section provide some initial insight into the typical behavior of norm ratios for random Fourier cosine sums (8), they do not indicate for what instances of f the smaller norm ratios are realized. Therefore, our next step is an attempt to understand the behavior of functions of the above type by forcing the signs of the normal coefficients. This approach is motivated by the fact that the worst-case behavior is observed if all signs of the coefficients c_k are equal. Throughout this section, we consider random functions of the form

$$g^{(m)}(x) = \sum_{k \in \Lambda} s_k \cdot |c_k| \cdot \sqrt{2} \cos(k\pi x), \quad (9)$$

where Λ and the coefficients c_k are defined as in Definition 1. Newly introduced are the sign coefficient factors $s_k \in \{-1, 1\}$ for $k \in \Lambda$, where we assume that $|\{k \in \Lambda : s_k = 1\}| = m$, for some integer $m \in \{0, \dots, |\Lambda|\}$. In other words, the superscript m in (9) determines the number of positive coefficients in the random Fourier cosine sum. Note, however, that the locations of the positive signs are randomly distributed among all of the involved mode functions.

In order to get a first impression of the effects of sign forcing on the behavior of random Fourier cosine sums, Figure 3 depicts five instances of $g^{(m)}$ for the parameter $\varepsilon = 10^{-2.5}$. In the simulations, the set of modes for which the sign s_k is positive gets chosen by a standard urn model. These first simulations lead to a number of observations.

Observation 7. *Consider the sample random Fourier cosine sums shown in Figure 3. In the associated Table 2, we have recorded a number of norm ratios for these five instances of $g^{(m)}$. In addition to the function value at zero, we consider the maximum norm over the interval $[0.2, 1]$, and the maximum norm over the whole interval $[0, 1]$, in each case normalized by the $L^2(0, 1)$ -norm of the function. These computations indicate the following:*

- *The function value $|g^{(m)}(0)|$ is more or less linearly decreasing as the sign parameter m increases from 0 to $\Lambda/2$.*

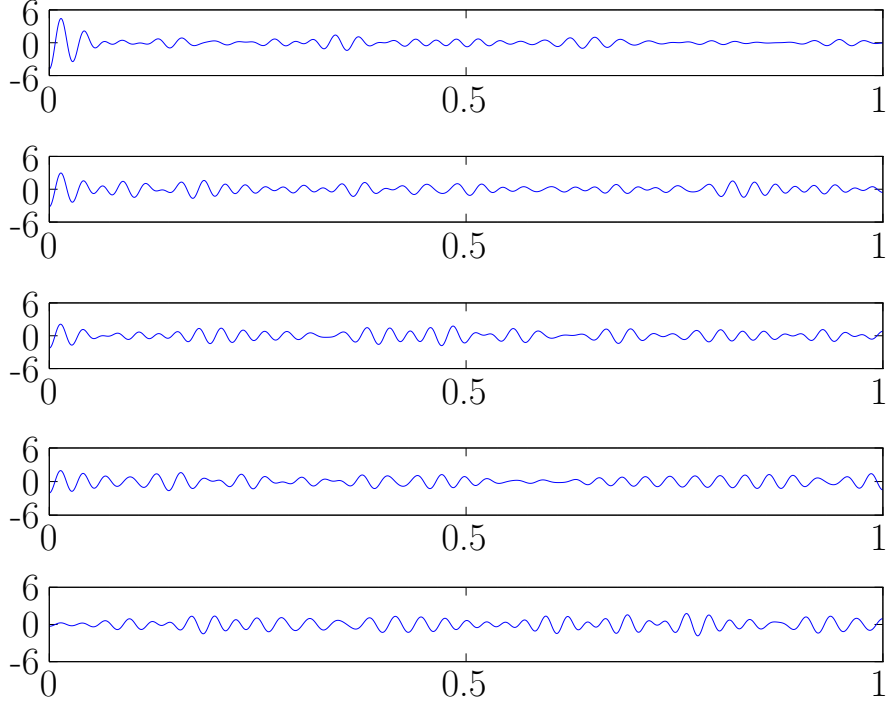


Figure 3: Sample random instances of the normalized functions $g^{(m)}/\|g^{(m)}\|_{L^2(0,1)}$ defined in (9) for the parameter value $\varepsilon = 10^{-2.5}$. In this case, the random sums involve $|\Lambda| = 33$ modes. From top to bottom the images correspond to the sign parameters $m = 0, 4, 8, 12, 16$.

m	$\frac{ g^{(m)}(0) }{\ g^{(m)}\ _{L^2(0,1)}}$	$\frac{\ g^{(m)}\ _{[0.2,1]}}{\ g^{(m)}\ _{L^2(0,1)}}$	$\frac{\ g^{(m)}\ _{L^\infty(0,1)}}{\ g^{(m)}\ _{L^2(0,1)}}$
0	4.8	1.4	4.8
4	3.2	1.5	3.2
8	2.3	1.8	2.2
12	2.0	1.5	2.0
16	0.3	1.8	1.8

Table 2: Specific norm ratios for the instances of $g^{(m)}$ shown in Figure 3. The table contains the size of the function value at zero, the maximum norm over the interval $[0.2, 1]$, as well as the maximum norm over the whole interval $[0, 1]$, in each case normalized by the $L^2(0, 1)$ -norm of the function.

- The largest function values over the interval $[0.2, 1]$ seem to be more or less of the same order as m changes, with fluctuations only due to the presence of noise.
- For small values of m , the maximum norm of $g^{(m)}$ over the interval $[0, 1]$ is attained at

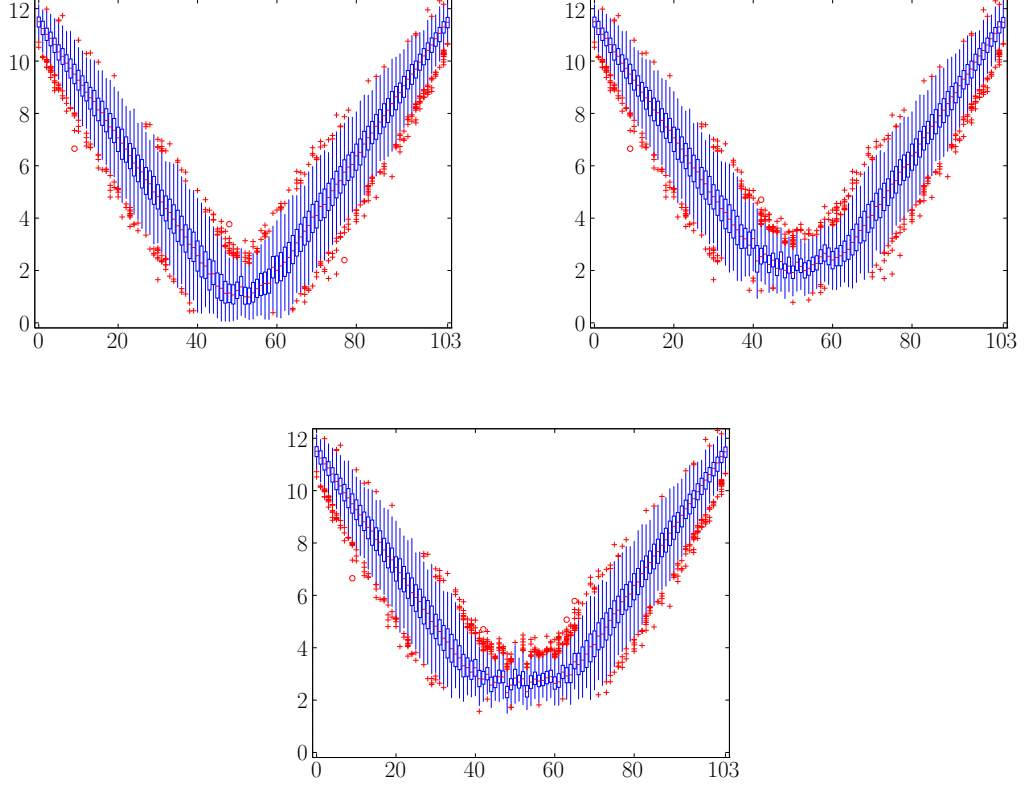


Figure 4: Boxplot of Monte Carlo simulations to determine typical values of the restricted norm ratios $\|g^{(m)}|_{[0,c]}\|_{L^\infty(0,1)}/\|g^{(m)}\|_{L^2(0,1)}$ for varying values of c . In all images, the horizontal axis represents the sign forcing parameter m , and for each m we performed $N = 150$ simulations. All graphs are for $\varepsilon = 10^{-3}$, and from top left to bottom middle we consider the cases $c = 0.01$, $c = 0.1$, and $c = 0.3$, respectively.

the point $x = 0$, while for larger values of m the largest function value occurs somewhere in the interval $[0.2, 1]$.

While the above observation is merely based on a few sample functions, it does seem to indicate that depending on the number m of positive coefficient signs s_k , the maximum norm of typical functions $g^{(m)}$ is either attained at the left domain boundary, or somewhere away from this boundary point.

At first glance, the above observation might seem surprising. For a fairly large contiguous range of sign forcing parameters which start at $m = 0$, the maximum norm of the random Fourier cosine sum f is attained exactly at the left boundary point, while from some m -value onwards, the maximum is suddenly observed in the interval $[0.2, 1]$. To study this phenomenon further, we performed Monte Carlo simulations to determine typical values of the restricted norm ratios $\|g^{(m)}|_{[0,c]}\|_{L^\infty(0,1)}/\|g^{(m)}\|_{L^2(0,1)}$ for varying intervals $[0, c]$. For three different values of c and every value of m between 0 and $|\Lambda|$, we determined the norm ratios

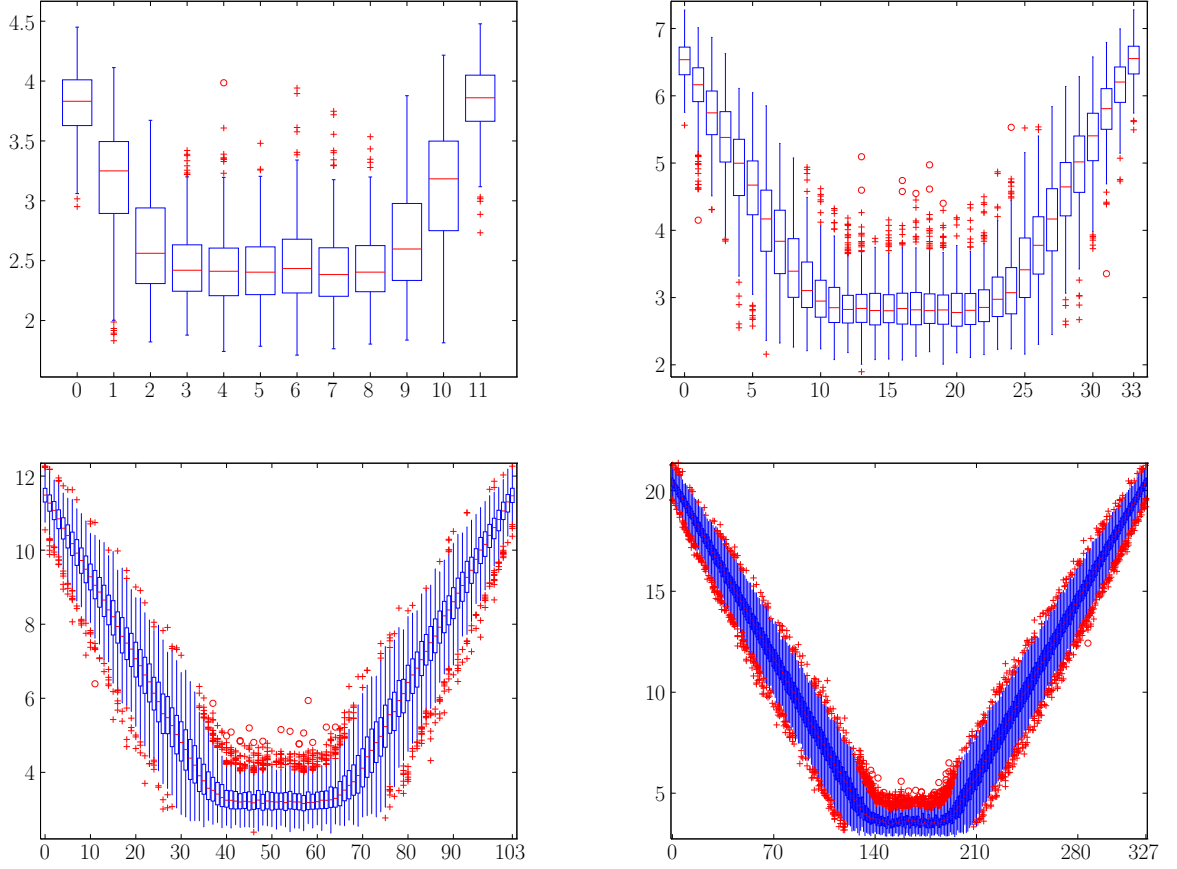


Figure 5: Boxplots of the norm ratios $\|g^{(m)}\|_{L^\infty(0,1)}/\|g^{(m)}\|_{L^2(0,1)}$ determined via Monte Carlo simulations with sample size $N = 1000$ for each m -value. From top left to bottom right the images correspond to the parameter values $\varepsilon = 10^{-2}$, $10^{-2.5}$, 10^{-3} , and $10^{-3.5}$, respectively. While the vertical axis measures the norm ratios, the horizontal axis represents $m+1$, where m is the sign forcing parameter ranging from 0 to $|\Lambda|$. All four graphs resemble “tubs,” with linearly growing sides and flat bottoms. Notice that while the ratio values at the bottom seem to vary only slightly with ε , the upper reaches of the sides increase with decreasing ε .

for $\varepsilon = 10^{-3}$ via $N = 150$ simulations. The results are shown in the boxplots of Figure 4. Notice that for $c = 0.01$, the normalized maximum norm over the interval $[0, c]$ decays linearly from about 11.5 to almost zero, as m ranges from zero to $|\Lambda|/2$. As m increases further, the behavior reverses. In this case, one would expect that the maximum norm closely resembles the behavior of $g^{(m)}$ at $x = 0$, due to the smallness of the interval. If instead of $c = 0.01$ we consider intervals with right endpoint $c = 0.1$ or $c = 0.3$, the norm ratios do not get as close to zero as before. In fact, they seem to bottom out at about 3. We have observed that as c increases beyond around $c \approx 0.2$, the bottom horizontal part shows hardly any change anymore.

n	$\varepsilon = 10^{-n}$	$\mathbb{E} \frac{ g^{(0)}(0) }{\ g^{(0)}\ _{L^2(0,1)}}$	$\mathbb{E} \frac{\ g^{(\Lambda /2)}\ _{L^\infty(0,1)}}{\ g^{(\Lambda /2)}\ _{L^2(0,1)}}$
2	0.01	4	2.5
2.5	0.003162	7	2.8
3	0.001	11	3.0
3.5	0.0003162	21	3.2

Table 3: Quantitative information for the tub plots in Figure 5. The third column gives the expected value of the ratio $|g^{(0)}(0)|/\|g^{(0)}\|_{L^2(0,1)}$, which corresponds to the height of the linear tub sides, while the fourth column represents the heights of the tub bottoms. The latter value is given by $\|g^{(m)}\|_{L^\infty(0,1)}/\|g^{(m)}\|_{L^2(0,1)}$ for $m = |\Lambda|/2$.

Combined, Figures 3 and 4 indicate that in order to study the maximum norm behavior of random Fourier cosine sums, it makes sense to relate the norm ratios to the number m of positive coefficients. As a final numerical experiment, we created plots similar to the ones in Figure 4, but this time for $c = 1$ and varying ε -values. The results from these Monte Carlo simulations are shown in Figure 5, and associated quantitative numerical values can be found in Table 3. For this experiment, we have performed Monte Carlo simulations with sample size $N = 1000$ for each m -value, and we considered the parameter values $\varepsilon = 10^{-2}$, $10^{-2.5}$, 10^{-3} , and $10^{-3.5}$, from top left to bottom right, respectively. As before, the vertical axis measures the norm ratios, while the horizontal axis represents $m + 1$, where m is the sign forcing parameter ranging from 0 to $|\Lambda|$. We would like to point out the striking similarity between the plot for $\varepsilon = 10^{-3}$ with the last image in Figure 4 — increasing the value of c from 0.3 to 1 has hardly any effect on its shape.

The four plots in Figure 5 share some interesting common features. All four graphs resemble “tubs,” with linearly decaying or growing sides and flat bottoms. The ratio values at the bottom of the tubs seem to vary only slightly with ε , whereas the upper reaches of the sides increase sharply with decreasing ε . This leads to the following observation.

Observation 8. *The largest norm ratio values are achieved when there is a strong dominance of one sign in the coefficients, i.e., most coefficients are positive or most are negative. This occurs close to the extreme values $m = 0$ and $m = |\Lambda|$. If this sign dominance decreases, the observed norm ratios decline approximately linearly up to the point where they reach a more or less constant level. The graphs are clearly symmetric with respect to $m = |\Lambda|/2$, due to our definition of $g^{(m)}$ in (9).*

Together with our observations surrounding Figure 3 this makes the case for the following scenario. For strongly asymmetric sign distributions, where for example all signs are positive or all are negative, the global maximum of the function $g^{(m)}$ occurs at $x = 0$, and in this case, one observes linear norm ratio decay as the sign distribution becomes more even. In the latter case, the function value at $x = 0$ is dominated by the function behavior away from the left endpoint of the domain. Consequently, the maximum is attained somewhere in the interior of the domain, and the maximum norm ratio stays more or less constant.

While the next two sections will be devoted to a more quantitative explanation of the

above observations, we close this section with a brief remark on the likelihood of encountering asymmetric sign distributions.

Remark 9. *As we will see in more detail later, the norm ratios observed in the middle of the tubs shown in Figure 5 are precisely the norm ratios that are responsible for typical instances of the random Fourier cosine sum f defined in (8). One can readily see that the sign distribution of the sequence $s_0, \dots, s_{|\Lambda|}$ follows a standard binomial distribution. In other words, sign distributions with m -values close to 0 or $|\Lambda|$ are extremely unlikely, while distributions with m close to $|\Lambda|/2$ are most probable. If we now assume that m is not chosen by us, but rather assigned randomly according to a binomial distribution, then the probability of the sign forcing parameter m taking a value along the flat tub bottom is given by an expression of the form*

$$\mathbb{P}(\ell \leq m \leq r) = \sum_{m=\ell}^r \text{Bin}(|\Lambda|, 0.5, m) ,$$

where ℓ and r denote the left and right endpoints of the bottom part of the tub. For each of the ε -values used in Figure 5, this probability can be computed as 0.9077, 0.9887, 0.9999, and almost 1, from top left to lower right, respectively. In other words, as ε decreases, the probability that a random Fourier cosine sum has a sign forcing parameter m which lies in the bottom of the tub is basically one — and this explains why typical f exhibit small maximum norm ratios.

3.2 The Role of the Left Endpoint of the Domain

Our simulations have already shown that the left endpoint of the interval $G = [0, 1]$ plays a special role in the formation of the maximum norm of a random Fourier cosine sum. Since this special role seems to occur only for strongly asymmetric sign distributions, we consider in the present section the case where all signs are equal. For the sake of definiteness, we assume that all signs s_k are equal to +1, and in this case the random Fourier cosine sum is given by

$$g^{(|\Lambda|)} = \sum_{k \in \Lambda} |c_k| \cdot \sqrt{2} \cos(k \cdot \pi \cdot x) .$$

Since the cosine functions all attain their maximum value 1 at $x = 0$, one can easily see that the maximum norm of $g^{(|\Lambda|)}$ is given by

$$\left\| g^{(|\Lambda|)} \right\|_{L^\infty(0,1)} = g^{(|\Lambda|)}(0) = \sqrt{2} \cdot \sum_{k \in \Lambda} |c_k| .$$

The sum of the absolute values of the standard normally distributed coefficients c_k is half-normally distributed, and it therefore has the expected value $|\Lambda| \cdot \sqrt{2/\pi}$ with variance $|\Lambda|$. In other words, one has

$$\mathbb{E} \left\| g^{(|\Lambda|)} \right\|_{L^\infty(0,1)} = \frac{2|\Lambda|}{\sqrt{\pi}} .$$

We now turn our attention to the $L^2(0, 1)$ -norm of the function $g^{(|\Lambda|)}$. Due to the orthonormality of the basis functions e_k , this norm can be computed via $\|g^{(|\Lambda|)}\|_{L^2(0,1)}^2 = \sum_{k \in \Lambda} c_k^2$.

The last sum is distributed according to a χ^2 -distribution with $|\Lambda|$ degrees of freedom. As mentioned several times, our interest in the norm ratios is their behavior as $\varepsilon \rightarrow 0$, and therefore we focus on the case that the number of degrees of freedom is large. In this situation, the above random variable becomes indistinguishable from a normal random variable with mean value $\mu = |\Lambda|$ and variance $\sigma^2 = 2|\Lambda|$. But even more can be said. The $L^2(0,1)$ -norm of the function $g^{(|\Lambda|)}$ follows a χ -distribution with

$$\text{mean value} \quad \mu = \sqrt{2} \cdot \frac{\Gamma\left(\frac{|\Lambda|+1}{2}\right)}{\Gamma\left(\frac{|\Lambda|}{2}\right)} \sim \sqrt{|\Lambda|} \quad \text{and variance} \quad \sigma^2 = |\Lambda| - \mu^2.$$

Note that the mean value μ is proportional to $\sqrt{|\Lambda|}$ with proportionality constant 1, which can easily be deduced from Stirling's formula. This in turn implies that the variance σ^2 does in fact grow much slower than $|\Lambda|$. In other words, as a rule of thumb we can assume that the L^2 -norm of $g^{(|\Lambda|)}$ satisfies $\|g^{(|\Lambda|)}\|_{L^2(0,1)} \approx \sqrt{|\Lambda|}$ with little variation.

The above discussion finally allows us to estimate the norm ratio for the function $g^{(|\Lambda|)}$. We expect that in fact

$$\frac{\|g^{(|\Lambda|)}\|_{L^\infty(0,1)}}{\|g^{(|\Lambda|)}\|_{L^2(0,1)}} \approx \frac{2\sqrt{|\Lambda|}}{\sqrt{\pi}}. \quad (10)$$

In the right-most column of Table 1 we have tabulated the values of the fraction on the right-hand side. These are in remarkable agreement with the numerically determined values shown in Table 3, see also Table 2.

What about values of the sign forcing parameter m which are different from $|\Lambda|$ or 0? The property that the maximum norm of $g^{(m)}$ is attained at $x = 0$ is somewhat stable, even if not all signs s_k are equal to +1, but only a majority of them. This is due to the fact that the point $x = 0$ is the only point in the interval G where all peaks of the cosine basis functions are at exactly the same spot, or in other words, are in phase. If we therefore consider $m \neq 0$, but still suppose that $\|g^{(m)}\|_{L^\infty(0,1)} = |g^{(m)}(0)|$, then one can easily see that $\|g^{(m)}\|_{L^\infty(0,1)}$ is — up to a factor $\sqrt{2}$ which comes from the normalization of the e_k — still half-normally distributed with expected value $\mu = (|\Lambda| - 2m) \cdot \sqrt{2/\pi}$, and this implies that

$$\mathbb{E} \left\| g^{(m)} \right\|_{L^\infty(0,1)} = (|\Lambda| - 2m) \cdot \frac{2}{\sqrt{\pi}}.$$

Heuristically one would therefore expect that

$$\frac{\|g^{(m)}\|_{L^\infty(0,1)}}{\|g^{(m)}\|_{L^2(0,1)}} \approx \frac{2\sqrt{|\Lambda|}}{\sqrt{\pi}} - \frac{4m}{\sqrt{\pi|\Lambda|}}. \quad (11)$$

This heuristic formula does indeed describe the linear decay which was observed in Figure 4, particularly in the top left image. Since this image only considers a small interval to the right of $x = 0$, we have performed essentially a Monte Carlo simulation to determine the expected value of the random variable $g^{(m)}(0)$. We expect its expected value to decay linearly to 0 as m increases from 0 to $\Lambda/2$, and then increase again in a symmetric way. Note, however,

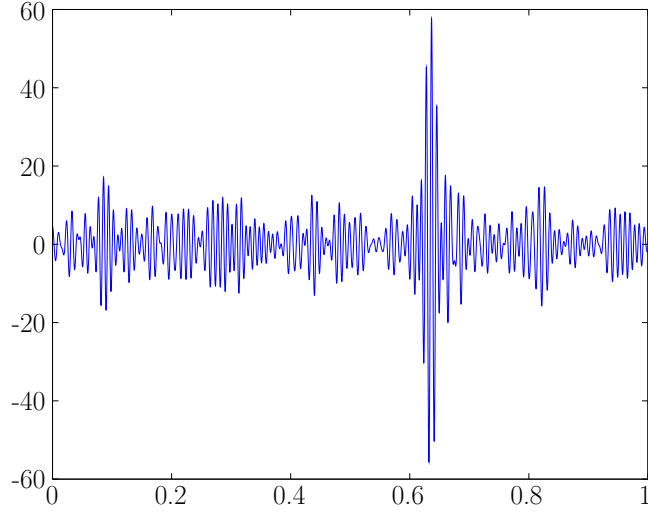


Figure 6: By forcing the signs of the coefficients c_k in the random Fourier cosine sum f according to very specific sign patterns, one can create worst-case behavior norm ratios at any point $\hat{x} \in [0, 1]$, not just at the left endpoint $x = 0$. The above image demonstrates this for the particular choice $\hat{x} = 2/\pi \approx 0.6366$.

that as we increase the size c of the interval $[0, c]$, the point $x = 0$ loses its importance as maximum norm defining argument for $m \approx |\Lambda|/2$. In this window, oscillations on the rest of the interval, which have the similar magnitude for all sign distributions, yield the norm of the function. The above-described effect is even more pronounced in the context of Figure 5, where we choose $c = 1$.

To summarize, we have shown in this section that the height and the linear behavior of the tubs shown in Figures 4 and 5 can be described accurately by the formulas (10) and (11), respectively. What still has to be explained is the horizontal behavior along the bottom of the tub, and this will be the subject of subsequent sections.

3.3 The Behavior at the Remaining Points

While the special role of the left endpoint $x = 0$ can easily be explained using the fact that all cosine basis functions are equal to their maximum at this point, it does make one wonder about the right end point $x = 1$. Also here, the basis functions realize their maximum norm, but this time the actual function value alternates between -1 and 1 . This implies that the random function $g^{(m)}$ follows the same probability law at both the right endpoint $x = 1$ and at the left endpoint of the interval G . However, this fact does not materialize in our previous simulations, since we considered events parametrized by the sign forcing variable m . In order for $x = 1$ to lead to high extremal values we would need to require that the signs s_k alternate as well, in order to compensate for the alternating signs of the basis functions.

The above reasoning can also be extended to arbitrary points in the domain $G = [0, 1]$.

For this, let $\hat{x} \in G$ be arbitrary. Our goal is to create random Fourier cosine sums f which exhibit large norm ratios $\|f\|_{L^\infty(0,1)}/\|f\|_{L^2(0,1)}$, but for which the maximum norm is attained at \hat{x} . For this, we need to imitate our considerations at the left endpoint. They were based on the idea that all of the signs of the values $c_k e_k(x)$ had to be the same. While for $x = 0$ this can be done explicitly, for $x = \hat{x}$ we need to understand the signs of $e_k(\hat{x}) = \sqrt{2} \cos(k\pi\hat{x})$. If we choose the sign of the coefficient c_k equal to the sign of $e_k(\hat{x})$, then the function values of f at $x = \hat{x}$ accumulate to a large positive value. Notice that this value does not automatically have to be the maximum norm of f , since the values $e_k(\hat{x})$ are usually not equal to ± 1 . However, At points $x \neq \hat{x}$ one would expect that the function values of $e_k(x)$ and $e_k(\hat{x})$ are generally out of sync, and therefore the computation of $f(x)$ should lead to numerous cancellations. This in turn should make it more difficult for $f(x)$ to reach the size of the function value $f(\hat{x})$. More precisely, consider an arbitrary point $\hat{x} \in G$. Then one can show that as long as $\cos(k\pi\hat{x}) \neq 0$ we have

$$\cos(k\pi\hat{x}) > 0 \quad \text{if and only if} \quad \ell_k(\hat{x}) := \max \left\{ l \in \mathbb{Z} : \frac{2l+1}{2k} \leq \hat{x} \right\} \quad \text{is odd} .$$

If we now define

$$\gamma_k(\hat{x}) := (-1)^{1+\ell_k(\hat{x})} ,$$

then, as long as $e_k(\hat{x}) \neq 0$, the statement $\gamma_k(\hat{x}) = +1$ is equivalent to $e_k(\hat{x}) > 0$. Finally, define $\gamma_k(\hat{x}) = 1$ if $\cos(k\pi\hat{x}) = 0$, and consider the random Fourier cosine sum

$$g_{\hat{x}}^{(m)}(x) = \sum_{k \in \Lambda} s_k \cdot |c_k| \cdot \gamma_k(\hat{x}) \cdot \sqrt{2} \cos(k\pi x) ,$$

where we assume that the number of signs $s_k \in \{\pm 1\}$ which are equal to $+1$ is given by m . Then one can show that the functions $g_{\hat{x}}^{(0)}$ and $g_{\hat{x}}^{(|\Lambda|)}$ do in fact exhibit exceedingly large norm ratios, see for example Figure 6 for the case $\hat{x} = 2/\pi$. In this way, we can also create functions which exhibit worst-case norm ratio behavior, but for which the maximum is attained in the interior of the domain — since the coefficient signs are in sync with the signs of $\cos(k\pi\hat{x})$.

4 Modeling Extreme Values

4.1 The Typical Oscillation Magnitude

This final section is devoted to understanding the formation of the plateaux or tub bottom in Figures 4 and 5, i.e., we will try to understand what determines the almost constant norm ratio in the regime where formula (11) no longer applies. This study focuses on the local extreme values of random Fourier cosine sums, their spatial distribution, and how precisely they are generated through the random sum. Moreover, we will develop a simplified model using binomial random variables to explain the main features of this process.

We begin by considering the following natural question. How does the function f develop its extreme values? Based on our discussion of the last section, it seems reasonable to expect that the formation of a local extreme point is likely near a point \hat{x} if many of the function values $e_k(\hat{x}) = \sqrt{2} \cos(k\pi\hat{x})$ have the same sign as the corresponding normal coefficients c_k . This can be quantified in the following way.

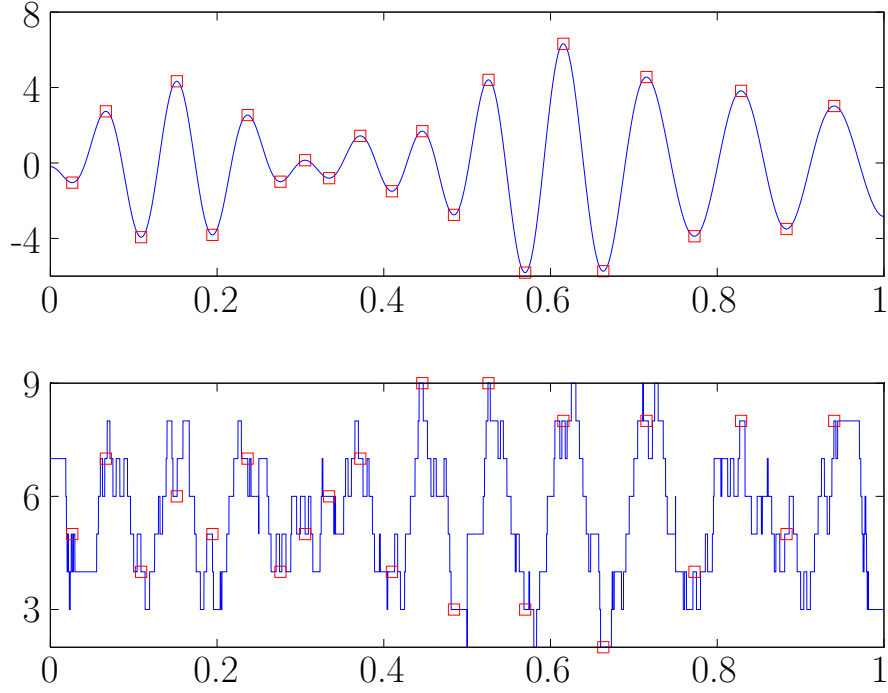


Figure 7: Relation between the match ratios and local extreme points. The first image shows a typical random Fourier cosine sum f for $\varepsilon = 10^{-2}$ with highlighted extremal values. The second image contains the match ratios for every point in the domain $G = [0, 1]$. One can detect a high correlation between properties of “being a local extremum” and “having an extreme match ratio.” For the shown images, the correlation factor is roughly 0.87.

Definition 10. We define the match number of a point $\hat{x} \in [0, 1]$ as

$$\text{match}(\hat{x}) = |\{k : \text{sgn}(c_k \cdot \cos(k\pi\hat{x})) = 1\}| ,$$

and the match ratio as its normalized equivalent given by

$$\overline{\text{match}}(\hat{x}) = \frac{\text{match}(\hat{x})}{|\Lambda|} \in [0, 1] .$$

If a given point \hat{x} has a high match number, close to $|\Lambda|$, then many of the basis functions e_k are multiplied by a coefficient c_k of the same sign so that the sum attains a high value. If a point has a low match number, i.e., close to 0, then most products $c_k e_k(\hat{x})$ are negative, and thus $f(\hat{x})$ becomes highly negative.

The suspected relation between match ratio and local extreme values can be observed in numerical simulations, see Figures 7 and 8. These computations have consistently resulted in average correlation factors over 0.8 between local extreme values and the match ratio.

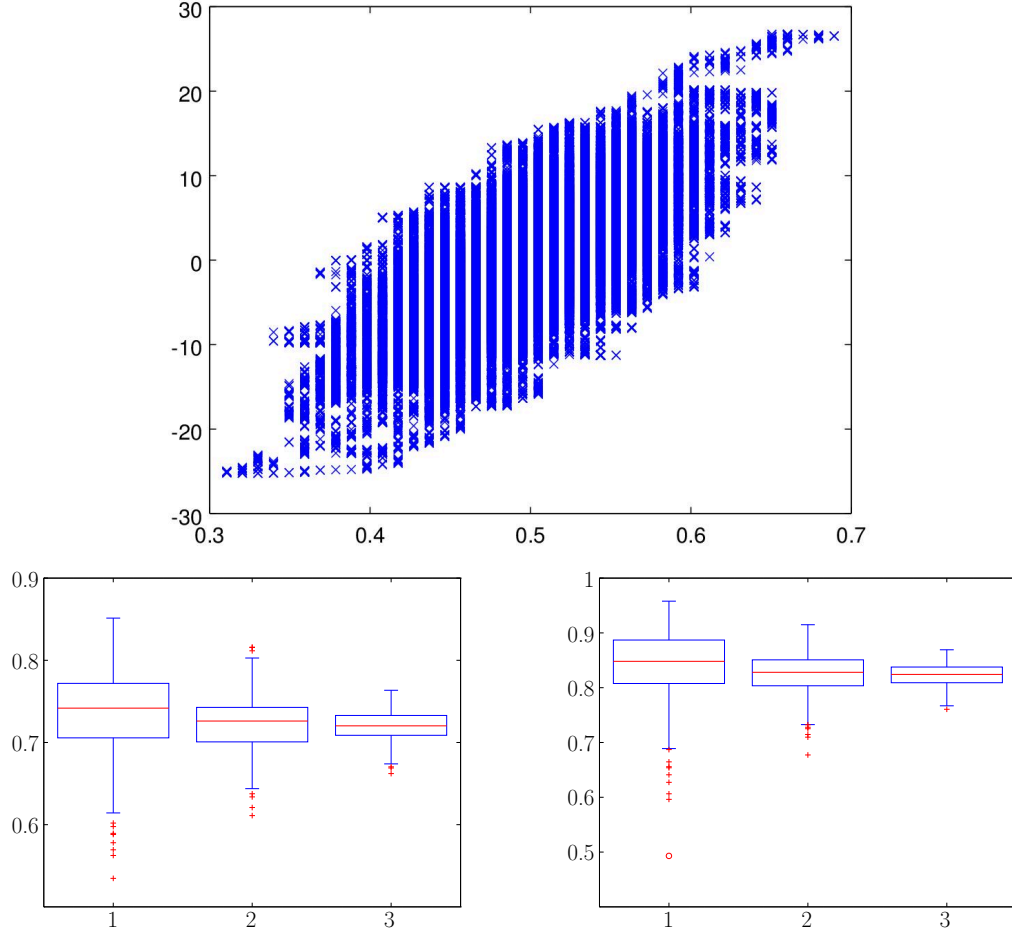


Figure 8: Understanding the relation between the match number and local extrema. The top image shows a scatter plot of the match ratio (horizontal axis) and the function value (vertical axis) for a fine grid of x -values in a numerically simulated Fourier cosine sum f with $\varepsilon = 10^{-3.5}$. The image indicates a high correlation between both quantities. The images on the bottom row depict boxplots of the correlation coefficients of 500 simulations analogous to the top panel, each time for $\varepsilon = 10^{-2}$, $\varepsilon = 10^{-2.5}$, and $\varepsilon = 10^{-3}$. The left picture depicts correlation of function value and match number in any point, the right picture shows the correlation only in extremal values.

We now turn our attention to the spatial distribution of local extrema. Their number is bounded above by the highest wave number of the involved cosine basis functions e_k , and bounded below by the lowest such wave number. In order to see this, note that the critical points of f are the zeros of its derivative, which is a Fourier sine function. The statement then follows from a classical result [13, Theorem 6.2, p. 35]. This leads to the following observation.

Observation 11. *Empirical simulations show that local extreme values are almost equidis-*

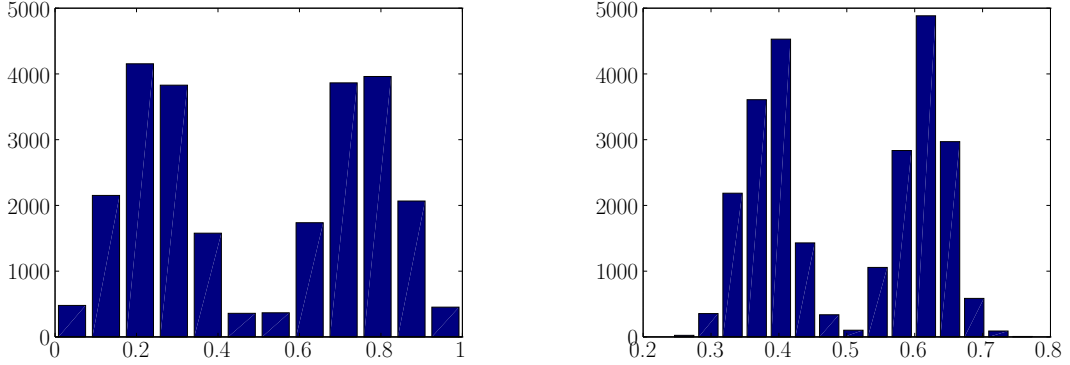


Figure 9: Histogram plot of the match ratio of the global extremum of the random Fourier cosine sum f from $N = 50000$ Monte Carlo simulations. The left image is for $\varepsilon = 10^{-2}$ while the right panel shows the case $\varepsilon = 10^{-3}$.

tantly distributed over the interval $G = [0, 1]$, with characteristic distance proportional to $1/\bar{k}$, where $\bar{k} \approx (k^\ominus + k^\oplus)/2$ is the average mode wave number, see also (6).

The observation shows that the function f has only about \bar{k} opportunities to generate a large $L^\infty(0, 1)$ -norm value. Moreover, in the direct vicinity of a local extremum there cannot be a second one, since the involved cosine basis functions oscillate too quickly. This indicates that in general, another local extremum can only be observed after a characteristic distance which is proportional to $1/\bar{k}$.

Suppose now that we have found a local extremum of f at the point \hat{x} . The signs of the cosine basis function values $e_k(\hat{x}) = \sqrt{2} \cos(k\pi\hat{x})$ are distributed over the modes in a more or less random fashion, which in fact is chaotic in a discrete dynamical systems sense. Apart from points of resonance, one would essentially expect equal numbers of positive and negative signs. These basis functions are then multiplied by the random coefficients c_k , which are standard normally distributed. From our previous discussion one can infer that the magnitude of the function value of f is larger if the fit between the signs of the cosine basis functions and the signs of the coefficients c_k is large as well, i.e., if the match number is either large or small. In addition to this requirement for the match number, the size of the function value of f is also affected by the magnitude of the random coefficients c_k .

Unfortunately, extremely large or small match numbers are rare events, since we can assume that they follow a binomial distribution. This means that match ratios equal to 0 or 1 occur with probability $2^{-|A|}$, while the most likely event is a match ratio of $1/2$, which usually leads to a function value close to 0 due to cancellations. Nevertheless, even slight variations from this match ratio value quickly result in much higher function values.

Observation 12. *Essentially, the size of the $L^\infty(0, 1)$ -norm is the result of a trade-off between sharply declining binomial probabilities, which model the likelihood of match numbers, and the creation of function values of large size through match number ratios away from the center ratio $1/2$. This trade-off is visualized in Figure 9, which shows histograms of the match ratio of the global extremum of f from Monte Carlo simulations for $\varepsilon = 10^{-2}$ and $\varepsilon = 10^{-3}$.*

4.2 A Model for the Magnitude of Extreme Values

We still have to understand what the characteristic magnitude of the middle part of the plots in Figure 5 is. For this, we will develop a model which captures the essential aspects of the generation of extreme values. This will be based on our observations of the previous sections.

As we have already seen, extrema are formed at approximately equidistant points in the domain, with average distance roughly equal to $1/\bar{k}$, where we defined $\bar{k} = (k^\ominus + k^\oplus)/2$. In other words, in general the random Fourier cosine sum f has about \bar{k} local minima and maxima. Since both k^\ominus and k^\oplus are of the same order in ε , the same can be said about their average \bar{k} . In order to develop our model, we now fix some $x \in [0, 1]$ and define the two index sets

$$\Lambda_1 = \{k \in \Lambda : \text{sgn}(c_k \cdot \cos(k\pi x)) = 1\} \quad \text{and} \quad \Lambda_2 = \Lambda \setminus \Lambda_1 .$$

This immediately implies the identity

$$\sum_{k \in \Lambda} c_k \cdot \cos(k\pi x) = \sum_{k \in \Lambda_1} |c_k| \cdot |\cos(k\pi x)| - \sum_{k \in \Lambda_2} |c_k| \cdot |\cos(k\pi x)| ,$$

where for the moment we remove the normalization factor $\sqrt{2}$ in the cosine basis functions for the sake of simplicity. It follows from a standard result in discrete dynamical systems that the function values $\cos(k\pi x)$ are ergodic with respect to iteration in k as long as the product πx is irrational. We can therefore model each term $|\cos(k\pi x)|$ by a random variable which is drawn according to the average magnitude of sinusoidal functions on their positive regime, i.e., we can assume that

$$|\cos(k\pi x)| = \sin(\pi d_k) ,$$

where the random variables d_k are independent and uniformly distributed on the interval $[0, 1]$, to ensure the positivity of the function value. These random variables model the fact that the peaks of the cosine functions do not coincide exactly, so we have to account for imperfect summation on positivity sets. Using the central limit theorem, one then obtains the approximation

$$\sum_{k \in \Lambda_1} |c_k| \cdot \sin(\pi d_k) - \sum_{k \in \Lambda_2} |c_k| \cdot \sin(\pi d_k) \simeq \mathcal{N}(\mu, \sigma^2) ,$$

where

$$\begin{aligned} \mu &= (|\Lambda_1| - |\Lambda_2|) \cdot \mathbb{E}(|c_k| \sin(\pi d_k)) = (|\Lambda_1| - |\Lambda_2|) \cdot \left(\frac{2}{\pi}\right)^{3/2} \quad \text{and} \\ \sigma^2 &= (|\Lambda_1| + |\Lambda_2|) \cdot \text{Var}(|c_k| \sin(\pi d_k)) = |\Lambda| \cdot \left(\frac{1}{2} - \frac{8}{\pi^3}\right) . \end{aligned}$$

We now need to model how the mode index sets Λ_1 and Λ_2 are chosen. For each $x \in [0, 1]$ this will be accomplished according to the match number $M \sim \text{Bin}(|\Lambda|, 0.5)$. This yields updated formulas for the mean μ and variance σ^2 in the form

$$\mu = (2M - |\Lambda|) \cdot \left(\frac{2}{\pi}\right)^{3/2} \quad \text{and} \quad \sigma^2 = |\Lambda| \cdot \left(\frac{1}{2} - \frac{8}{\pi^3}\right) .$$

Our rationale for modeling the match number M by a binomial distribution can easily be explained. In every local extremum \hat{x} , the coefficient sequence $(c_k)_{k \in \Lambda}$ yields a sign distribution on the basis functions $\cos(k\pi\hat{x})$. Since we consider \hat{x} as being picked randomly in the interval $[0, 1]$, the ergodic property of the system of mainly non-resonant cosine functions gives another sequence of independent signs $(\cos(k\pi\hat{x}))_{k \in \Lambda}$. Thus, their product is also a mixture of signs, and we can assume that the number of positive signs is binomially distributed with probability parameter $1/2$.

We now take our simplified model one step further. Using the Moivre-Laplace theorem one can approximate the random variable $M - |\Lambda|/2$ by a normal distribution with mean zero and variance $|\Lambda|/4$. Hence, using the abbreviations $C_1 = 2(2/\pi)^{3/2}$ and $C_2 = 1/2 - 8/\pi^3$ we obtain

$$\begin{aligned} y_m &\sim \mathcal{N}(C_1(M - |\Lambda|/2), C_2|\Lambda|) \\ &\sim \mathcal{N}(\mu = \mathcal{N}(0, \sigma^2 = C_1^2|\Lambda|/4), \sigma^2 = C_2|\Lambda|) \\ &= |\Lambda|^{1/2} \cdot \mathcal{N}(\mu = 0, \sigma^2 = C_1^2/4 + C_2) \\ &= |\Lambda|^{1/2} \cdot \mathcal{N}(0, \sigma^2 = 1/2), \end{aligned}$$

where the second-to-last step is an elementary calculation. Note also that $C_1^2/4 + C_2 = 1/2$ holds. The above derivations can now be summarized and condensed into our simplified extreme value model.

Definition 13 (Simplified Extreme Value Model). *In order to draw the values (y_m) of the extreme values of a random Fourier cosine sum, we choose y_m as an independent copy of*

$$y_m \sim \mathcal{N}(\mu = 0, \sigma^2 = |\Lambda|/2),$$

and the match number approximation will be given by choosing M_m as an independent copy of

$$M_m \sim \mathcal{N}(\mu = |\Lambda|/2, \sigma^2 = 8|\Lambda|/\pi^3).$$

Moreover, in our model we treat the $L^2(0,1)$ -norm of the random Fourier cosine sum f as being fixed with value $\sqrt{|\Lambda|}$, see the discussion in Section 3.2. All of these choices are significant simplifications, but we will see later that they lead to a model which captures the key features of the extreme values. For abbreviation purposes, we define

$$\|f^{\text{MODEL}}\|_{L^\infty(0,1)} = \sqrt{2} \cdot \max_{m=1,\dots,k} |y_m| = \sqrt{2}|y_{\hat{m}}| \quad \text{and} \quad \|f^{\text{MODEL}}\|_{L^2(0,1)} = \sqrt{|\Lambda|}.$$

Notice that the extra factor $\sqrt{2}$ accounts for the normalization of the basis functions e_k .

Using numerical Monte Carlo simulations, we have tested the performance of the above model for a variety of different values of ε . The results can be found in Figures 10 through ??, and they demonstrate that both the match number and the absolute magnitude of local and global extrema are approximated fairly well. More precisely, Figure 10 compares the actual distribution of local extreme values with the ones generated by the simplified model in

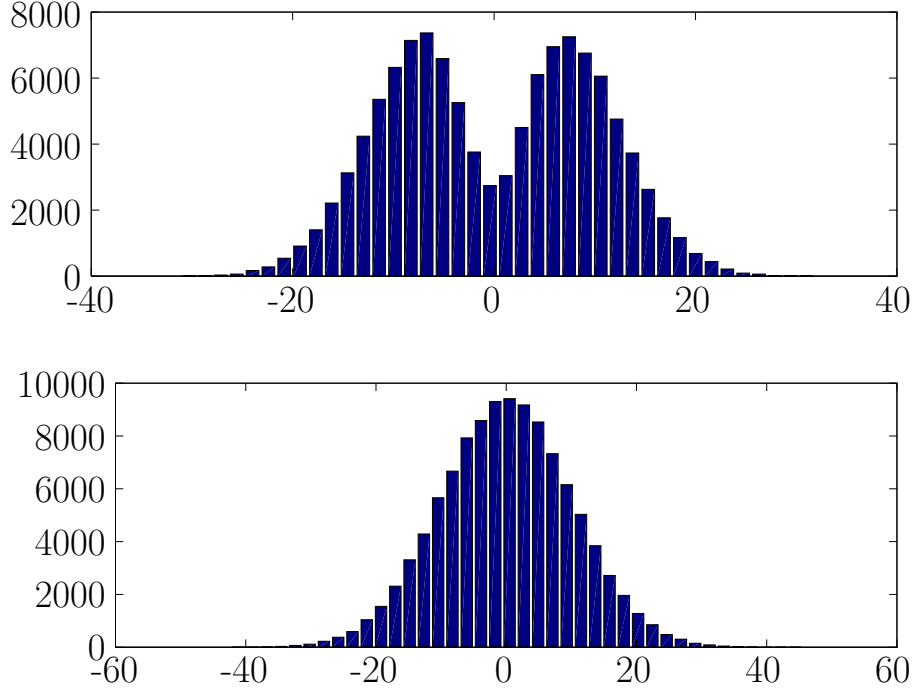


Figure 10: Comparison of the actual distribution of local extreme values (lower panel) with the ones generated by the model in Definition 13 (upper panel) for $\varepsilon = 10^{-3}$. Except for a neighborhood around zero, both yield similar distributions. Notice, however, that the extreme values near zero do not affect the $L^\infty(0, 1)$ -norm of f anyway.

Definition 13, while Figure 11 does the same for the match numbers of local extrema. Both of these figures consider the parameter $\varepsilon = 10^{-3.5}$. The remaining Figures 13 through ?? compare the actual global extreme values of the random Fourier cosine sum f to the ones generated by the simplified model for $\varepsilon = 10^{-2}$, $\varepsilon = 10^{-3}$, and $\varepsilon = 10^{-4}$, respectively.

4.3 Growth Rate of the Maximum Norm

Can we use the simplified model in Definition 13 to derive the height of the plateaux in Figure 5, and in particular its dependence on ε ? For this, notice that the Moivre-Laplace theorem can be used in combination with the strong law of large numbers to obtain a precise approximation result for the m -th local extremal values, which in the model are given by

$$\frac{y_m}{\|f^{\text{MODEL}}\|_{L^2(0,1)}} \sim \mathcal{N}(\mu = 0, \sigma^2 = 1/2)$$

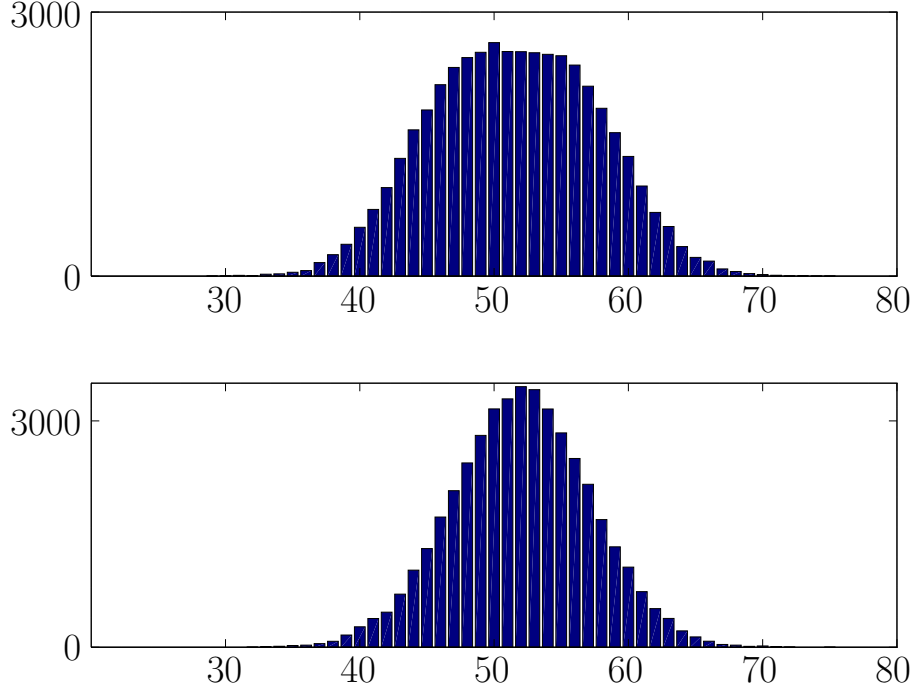


Figure 11: Comparison of the actual distribution of the match numbers of local extrema (upper panel) with the ones generated by the model in Definition 13 (lower panel) for $\varepsilon = 10^{-3}$.

Note that in this formulation, we again ignore the normalization factors $\sqrt{2}$, as they can be absorbed into the proportionality constant later on. We then obtain the approximation

$$\mathbb{P} \left(\max_{m=1, \dots, \bar{k}} \frac{|y_m|}{\|f^{\text{MODEL}}\|_{L^2(0,1)}} < t \right) = \prod_{m=1, \dots, \bar{k}} \mathbb{P} \left(\frac{|y_m|}{\|f^{\text{MODEL}}\|_{L^2(0,1)}} < t \right) \leq \left(\int_{-\infty}^t \frac{e^{-s^2}}{\sqrt{\pi}} ds \right)^{\bar{k}}.$$

The improper integral can be bounded below in the form

$$\int_{-\infty}^t \frac{e^{-s^2}}{\sqrt{\pi}} ds = 1 - \int_t^{\infty} \frac{e^{-s^2}}{\sqrt{\pi}} ds \geq 1 - C \int_t^{\infty} e^{-cs} ds = 1 - Ce^{-ct}$$

for every positive constant $c > 0$ and all sufficiently large t . If we now use Definition 13 and choose $t = \sqrt{2} \ln(1/\varepsilon)$, then one obtains from the above calculations the estimate

$$\mathbb{P} \left(\frac{\|f^{\text{MODEL}}\|_{L^\infty(0,1)}}{\|f^{\text{MODEL}}\|_{L^2(0,1)}} < t \right) = \left(\int_{-\infty}^{\ln(1/\varepsilon)} \frac{e^{-s^2}}{\sqrt{\pi}} ds \right)^{(\alpha^\oplus + \alpha^\ominus)/(2\varepsilon)} \geq (1 - C\varepsilon^c)^{D/\varepsilon},$$

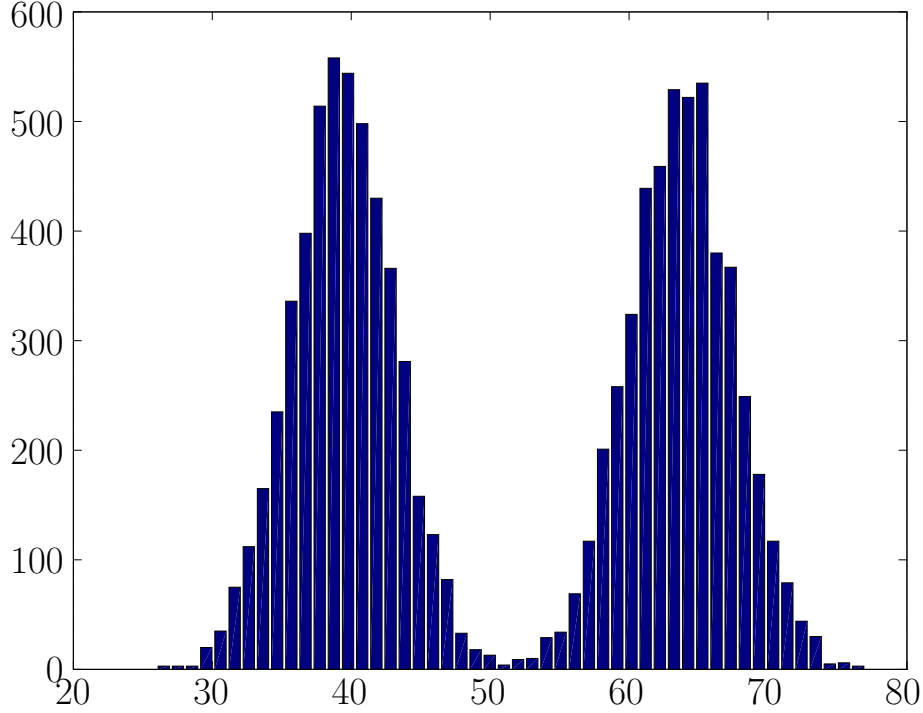


Figure 12: Histogram of the match numbers of global extrema. Compare with the upper panel in figure 11. A comparison with the model doesn't make sense as the match numbers do not correspond to model extrema.

see also (7). One can easily see that the term on the right-hand side satisfies

$$\lim_{\varepsilon \rightarrow 0} (1 - C\varepsilon^c)^{D/\varepsilon} = \lim_{\delta \rightarrow 0} (1 - \delta^c)^{E/\delta} = 1 \quad \text{for all } c > 1.$$

This finally furnishes the following result.

Theorem 14. *Consider the simplified extreme value model introduced in Definition 13. Then for any fixed constant $C > 0$ we have*

$$\mathbb{P} \left(\frac{\|f^{\text{MODEL}}\|_{L^\infty(0,1)}}{\|f^{\text{MODEL}}\|_{L^2(0,1)}} < C \log \varepsilon^{-1} \right) \rightarrow 1 \quad \text{as } \varepsilon \rightarrow 0.$$

Theorem 14 improves the estimate obtained in Theorem 6, but for the simplified extreme value model. In fact, numerical simulations indicate that the logarithmic bound describes the growth of the plateaux heights in Figure 5 precisely.

Before closing this section, we would like to point out a number of shortcomings of our simplified model. First of all, the model ignores any dependencies between close extrema.

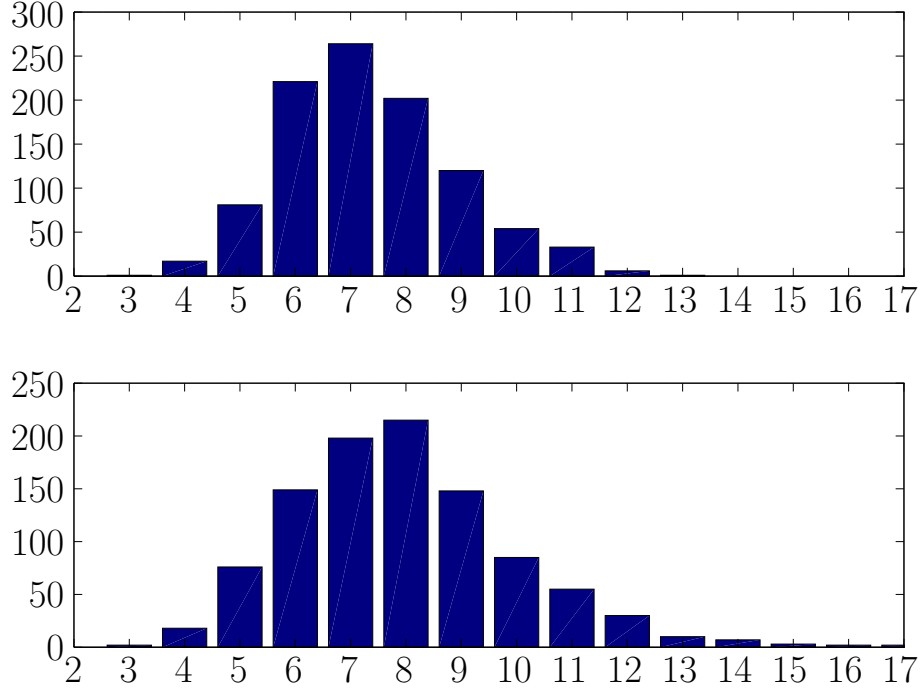


Figure 13: Comparison of the actual global extreme values (lower panel) with the ones generated by the model in Definition 13 (upper panel) for $\varepsilon = 10^{-2}$.

While this simplifies our model tremendously, it does not seem to alter the quality of its prediction in a significant way. Subsequent extrema are strongly dependent, but also of roughly the same magnitude. Since we are only interested in the order of magnitude of the norm ratio growth as $\varepsilon \rightarrow 0$, we do not expect any large negative effects.

Another shortcoming, however, is more serious. As shown in Figure 10, while the local extrema do indeed exhibit a binomially shaped match number distribution, the distribution of their function values differs from the model in a major point — only rarely are local extrema observed whose values are close to zero. For our purposes, however, this is not too important. We are interested in the behavior of the $L^\infty(0,1)$ -norm, and therefore in the global extremal value. The latter one is realized via local extrema with high match numbers. On the other hand, our modeling error only affects extremal values with low match numbers. For simulating and predicting the $L^\infty(0,1)$ -norm, this can be ignored. We refer the reader again to Figures 13 through ??.

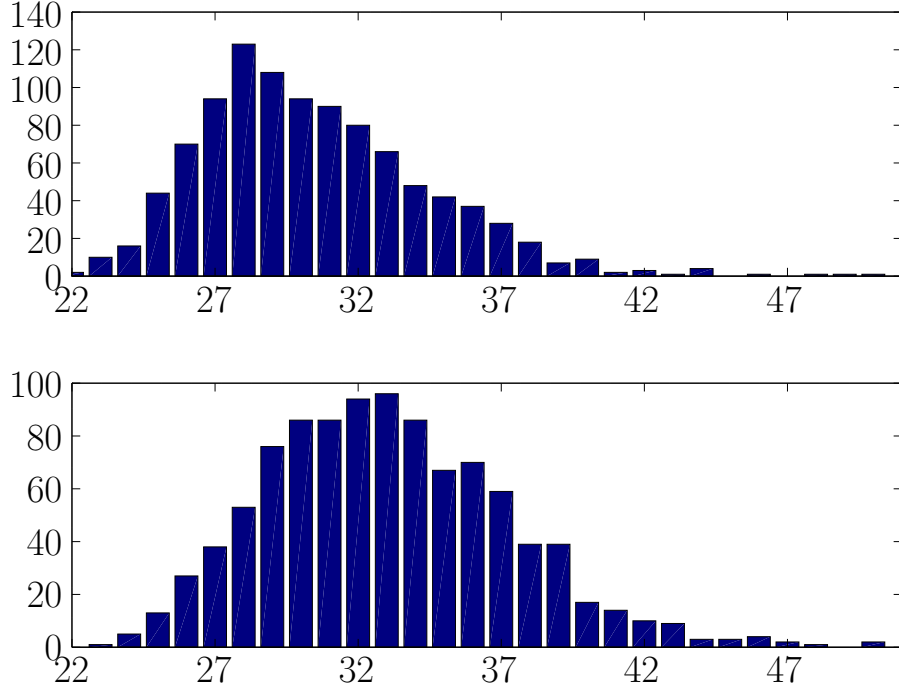


Figure 14: Comparison of the actual global extreme values (lower panel) with the ones generated by the model in Definition 13 (upper panel) for $\varepsilon = 10^{-3}$.

4.4 Generalization to Higher Dimensions

While the bulk of the paper considered the case of random Fourier cosine sums on one-dimensional domains, the extension to higher dimensions is not difficult. First the results of Section 2 hold almost verbatim with only minor modifications. In section 3 in case of a square or cube domain, the role of the boundary points is taken over by the corners, and, when we force the signs, we expect similar numerical results with a plateau in the middle. They would just be significantly more time consuming, as the number of terms in the series is on the order of ε^{-d} and grows with the dimension d .

Finally, we give a brief discussion of the simplified model derived in section 4. We only consider the case of a two-dimensional square domain, and leave the straightforward generalization to higher dimensions to the reader. Consider the domain $G = [0, 1]^2$ and define

$$\Lambda = \left\{ (k, \ell) \in \mathbb{N}^2 : k^\ominus \leq \sqrt{k^2 + \ell^2} \leq k^\oplus \right\},$$

as well as independent and identically distributed random normal variables $c_{k,\ell}$ for $(k, \ell) \in \Lambda$, with mean zero and variance one. Finally, define the random Fourier cosine sum in two

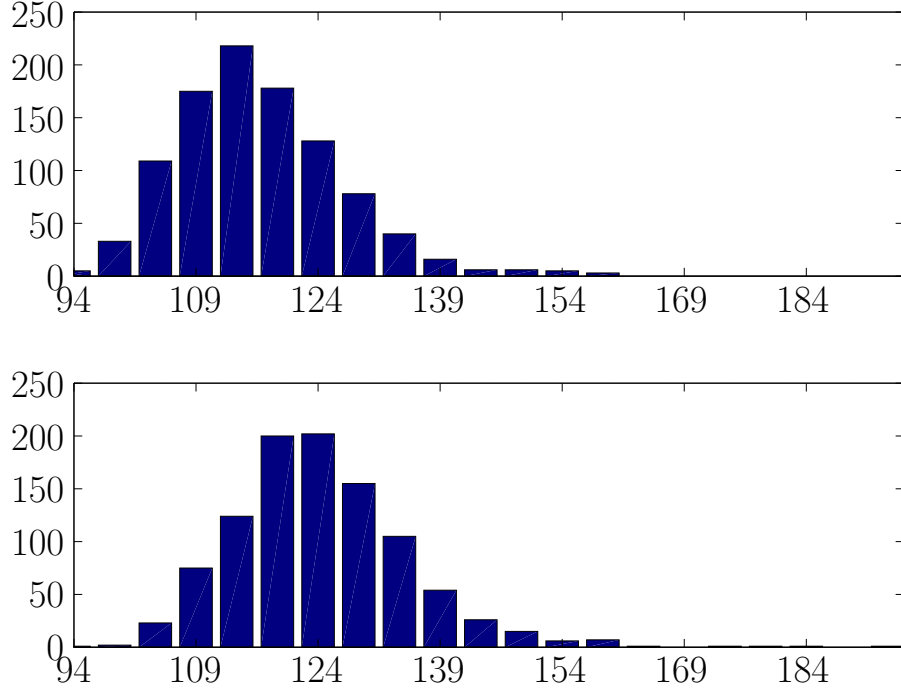


Figure 15: Comparison of the actual global extreme values (lower panel) with the ones generated by the model in Definition 13 (upper panel) for $\varepsilon = 10^{-4}$.

dimensions by

$$f(x, y) = \sum_{(k, \ell) \in \Lambda} c_{k, \ell} \cos(k\pi x) \cos(\ell\pi y) .$$

In this new situation, the index set is a quarter annulus. As before, the local extreme values can be modeled as

$$y_m \sim \sum_{(k, \ell) \in \Lambda_1} |c_{k, \ell}| \sin(\pi d_{k, \ell}) \sin(\pi \tilde{d}_{k, \ell}) - \sum_{(k, \ell) \in \Lambda_2} |c_{k, \ell}| \sin(\pi d_{k, \ell}) \sin(\pi \tilde{d}_{k, \ell}) ,$$

where Λ_1 and Λ_2 denote the modes for which the product $c_{k, \ell} \cos(k\pi x) \cos(\ell\pi y)$ is strictly positive or negative, respectively, where $(x, y) \in G$ is the location of a local extremum. Moreover, the random variables $d_{k, \ell}$ and $\tilde{d}_{k, \ell}$ are uniformly distributed in $[0, 1]$. Through elementary calculations similar to the ones in the one-dimensional case one obtains

$$y_m \sim \mathcal{N}(\mu, \sigma) \quad \text{with} \quad \mu = (|\Lambda_1| - |\Lambda_2|) \left(\frac{2}{\pi} \right)^{5/2} \quad \text{and} \quad \sigma^2 = |\Lambda| \left(\frac{3}{8} - \frac{2}{\pi^2} - \frac{2}{\pi^3} \right) .$$

As before we assume that $|\Lambda_1| - |\Lambda_2| = 2M - |\Lambda| \sim 2 \text{Bin}(|\Lambda|, 0.5) - |\Lambda| \sim \mathcal{N}(0, |\Lambda|/4)$. In

addition, the number of modes contained in Λ is now asymptotically given by

$$|\Lambda| \sim \frac{\pi ((\alpha^\oplus)^2 - (\alpha^\ominus)^2)}{4\varepsilon^2}.$$

Analogously to the one-dimensional proceeding, one can then derive

$$\frac{y_m}{\|f^{\text{MODEL}}\|_{L^2(G)}} \sim \mathcal{N}(0, C),$$

where C denotes some ε -independent constant, and the number of extrema is empirically given by

$$\bar{k}^2 = \frac{(k^\oplus + k^\ominus)^2}{4} = \frac{(\alpha^\oplus + \alpha^\ominus)^2}{4\varepsilon^2}.$$

Using the highest possible mode frequency we can now say that the number of extrema is bounded by $(k^\oplus)^2 \sim (\alpha^\oplus/\varepsilon)^2$. Hence, the probability distribution can be derived as above as

$$\mathbb{P} \left(\max_{m=1, \dots, \bar{k}^2} \frac{|y_m|}{\|f^{\text{MODEL}}\|_{L^2(G)}} < t \right) > \left(\int_{-\infty}^t C_1 e^{-s^2/C_2} ds \right)^{(\alpha^\oplus)^2/\varepsilon^2},$$

and as in Section 4.3, this yields an estimate for the $L^\infty(G)$ -norm growth rate in two dimensions, if one chooses $t = C \log \varepsilon^{-1}$. This implies

$$\lim_{\varepsilon \rightarrow 0} \mathbb{P} \left(\frac{\|f^{\text{MODEL}}\|_{L^\infty(G)}}{\|f^{\text{MODEL}}\|_{L^2(G)}} < C \log \varepsilon^{-1} \right) = 1,$$

where we assumed that $\|f^{\text{MODEL}}\|_{L^2(G)} = C\varepsilon^{-1}$ is roughly constant also in two dimensions.

Acknowledgements

D.B. would like to thank Vitaly Wachtel for fruitful discussions about Theorem 6. P.W. is thankful for the funding he received by Cusanuswerk. Finally, T.W. was partially supported by NSF grants DMS-1114923 and DMS-1407087.

References

- [1] R. Aurich, A. Bäcker, R. Schubert, and M. Taglieber. Maximum norms of chaotic quantum eigenstates and random waves. *Physica D*, 129:1–14, 1999.
- [2] Dirk Blömker, Stanislaus Maier-Paape, and Thomas Wanner. Spinodal decomposition for the Cahn-Hilliard-Cook equation. *Communications in Mathematical Physics*, 223(3):553–582, 2001.
- [3] Dirk Blömker, Stanislaus Maier-Paape, and Thomas Wanner. Phase separation in stochastic Cahn-Hilliard models. In Alain Miranville, editor, *Mathematical Methods and Models in Phase Transitions*, pages 1–41. Nova Science Publishers, New York, 2005.
- [4] Dirk Blömker, Stanislaus Maier-Paape, and Thomas Wanner. Second phase spinodal decomposition for the Cahn-Hilliard-Cook equation. *Transactions of the American Mathematical Society*, 360(1):449–489, 2008.

- [5] John W. Cahn. Free energy of a nonuniform system. II. Thermodynamic basis. *Journal of Chemical Physics*, 30:1121–1124, 1959.
- [6] John W. Cahn and J. E. Hilliard. Free energy of a nonuniform system I. Interfacial free energy. *Journal of Chemical Physics*, 28:258–267, 1958.
- [7] H. Cook. Brownian motion in spinodal decomposition. *Acta Metallurgica*, 18:297–306, 1970.
- [8] Richard Courant and David Hilbert. *Methods of Mathematical Physics*. Intersciences, New York, 1953.
- [9] Giuseppe Da Prato and Arnaud Debussche. Stochastic Cahn-Hilliard equation. *Nonlinear Analysis. Theory, Methods & Applications*, 26(2):241–263, 1996.
- [10] Giuseppe Da Prato and Jerzy Zabczyk. *Stochastic Equations in Infinite Dimensions*. Cambridge University Press, Cambridge, second edition, 2014.
- [11] Jonathan P. Desi, Evelyn Sander, and Thomas Wanner. Complex transient patterns on the disk. *Discrete and Continuous Dynamical Systems, Series A*, 15(4):1049–1078, 2006.
- [12] Jean-Pierre Kahane. *Some Random Series of Functions*. Cambridge University Press, Cambridge – London – New York, second edition, 1985.
- [13] Samuel Karlin. *Total Positivity*. Stanford University Press, Stanford, 1968.
- [14] J. S. Langer. Theory of spinodal decomposition in alloys. *Annals of Physics*, 65:53–86, 1971.
- [15] Stanislaus Maier-Paape and Thomas Wanner. Spinodal decomposition for the Cahn-Hilliard equation in higher dimensions. Part I: Probability and wavelength estimate. *Communications in Mathematical Physics*, 195(2):435–464, 1998.
- [16] Stanislaus Maier-Paape and Thomas Wanner. Spinodal decomposition for the Cahn-Hilliard equation in higher dimensions: Nonlinear dynamics. *Archive for Rational Mechanics and Analysis*, 151(3):187–219, 2000.
- [17] Thomas Runst and Winfried Sickel. *Sobolev Spaces of Fractional Order, Nemytskij Operators, and Nonlinear Partial Differential Equations*. Walter de Gruyter, Berlin, 1996.
- [18] Evelyn Sander and Thomas Wanner. Monte Carlo simulations for spinodal decomposition. *Journal of Statistical Physics*, 95(5–6):925–948, 1999.
- [19] Evelyn Sander and Thomas Wanner. Unexpectedly linear behavior for the Cahn-Hilliard equation. *SIAM Journal on Applied Mathematics*, 60(6):2182–2202, 2000.
- [20] Thomas Wanner. Maximum norms of random sums and transient pattern formation. *Transactions of the American Mathematical Society*, 356(6):2251–2279, 2004.